Chem. Rev. **2004,** *104,* 5449–5477

Magnetic TTF-Based Charge-Transfer Complexes

Toshiaki Enoki* and Akira Miyazaki

Department of Chemistry, Tokyo Institute of Technology, 2-12-1 Ookayama, Meguro-ku, Tokyo 152-8551, Japan

Received February 25, 2004

Contents

1. Introduction

The saga of magnetism started with the discovery of ferromagnetism of iron in the early stage of human history. Magnetism has contributed importantly to human life, as we can recollect the usefulness of the compass. In the modern era, magnetic materials have become indispensable as many tools we use for domestic purposes and in industrial activities. In addition to the practical uses of magnets, especially ferromagnets, magnetism is one of the most essential issues in basic physics and chemistry, which deals with the behavior of magnetic moments in solids. In this decade, the knowledge gained in the basic science has opened new trends of magnetism in the development of the cutting-edge electronic device applications. Among these, molecule-based magnets[1–9] are considered to be future-promising from several viewpoints. In molecules, the concept of molecular design works effectively in developing magnetic materials intentionally. Actually, the various internal degrees of freedom that individual molecules possess are available for designing functionality in the molecule, in which magnetism is one of the important features. Optical active magnets can be built by incorporating

Toshiaki Enoki was born in 1946 and received his Ph.D. in 1974 from Kyoto University, Japan. He was a Research Associate at the Institute for Molecular Science (1977–1987) and a Visiting Scientist at Massachusetts Institute of Technology in 1984. In 1987, he was appointed to the position of Associate Professor of the Department of Chemistry at Tokyo Institute of Technology, and he is now a full Professor. He was a Visiting Professor at the University of Rennes I in 2000 and at the Institute for Molecular Science (2003–2004). His research interests include physical chemistry, especially molecular magnets and conductors. He has been investigating magnetic organic charge-transfer complexes and carbon nanomaterials.

Akira Miyazaki was born in 1966 and received his Ph.D. in 1998 from the University of Tokyo, Japan. Since 1992, he has worked as a Research Associate of the Department of Chemistry at Tokyo Institute of Technology. His research interests include physical chemistry, especially molecular hybrid systems such as molecular conducting magnets. He has been investigating magnetic organic radical ion salts.

---

* Telephone: 81-3-5734-2242. Fax: 81-3-5734-2242. E-mail address: tenoki@chem.titech.ac.jp.

10.1021/cr0306438 CCC: $48.50

the optical function into molecular magnets.[10−12] Magnetic sensing probes can be produced when chemical functions are introduced into magnetic molecules. Electron-transfer functions can also be added to molecular magnets to give conducting, metallic, or even superconducting magnetic molecular systems.[2,13−15] Here, the concerted cooperation of conduction carriers and magnetic moments is expected to give unconventional magnetic features that have not been obtained in traditional magnetic materials, in which the interaction between conduction carriers and magnetic moments, the so-called s−d interaction, plays an important role in producing strong metal magnets such as ferromagnetic iron. The multifunctionality in magnetic molecules is expected to provide new ingredients in electronic molecular devices.

The simplicity of chemical modifications in molecules or molecular assemblies is advantageous in magnetic materials' design, when we take molecules as building blocks. The addition of functional groups, the substitution of part of the molecule, the modifications of molecular structures, and so on can vary the magnetic features, chemical activities, and shape of the molecules. The arrangements of molecules in 1-, 2-, and 3-dimensional (1D, 2D, and 3D) frameworks or in a cluster form produce molecule-based magnetic systems, which are interesting from the points of view of systematic and comprehensive investigations of magnetism in basic physics and also for applications of magnetic materials. Indeed, low-dimensional magnetic systems have provided good models with which physicists enjoy investigating statistical physics issues, such as low-dimensional magnetism, the Haldane quantum spin chain, the spin Peierls transition, spin ladders, and so on.[5,16,17] In recent works, the tunneling phenomena in single-molecule magnets,[18−20] which consist of clustered magnetic species, have been intensively investigated as a new topic in physics and also for potential applications to molecular devices.

Molecule-based ferromagnetism is also among the perspectives of molecular magnets, as the substitute for existing ferromagnetic materials or even more advanced ferromagnets. The discovery of the first organic ferromagnet, *p*-NPNN (=2-(4-nitrophenyl)-4,4,5,5-tetramethyl-4,5-dihydro-1*H*-imidazolyl-1-oxy-3-oxide),[21−23] has stimulated the race to find organic ferromagnetic materials. The trials for searching high-T_c organic ferromagnets are expected to bridge the gap between the fundamental work and the future device applications.

Among the molecule-based magnets, the family of charge-transfer complexes is one of the important classes of materials in fundamental magnetic chemistry and physics. The charge transfer from donor to acceptor produces electrons that play a role in the magnetism of the complexes. In the history of organic charge-transfer complexes, organic conductors have been intensively and comprehensively investigated so far, in which TTF-type molecules have been most popular in donor molecules.[24−26] The flat-shaped molecules tend to form low-dimensional arrangements in which π-electron carriers work to give a large variety of electronic phases such as charge density waves, spin density waves, or charge localization, metallic, or even superconducting phases. Designing molecular magnets on the basis of charge-transfer complexes can give a large variety of magnetic systems, in which π-electrons play an important role. In the present review, the works on magnetic TTF-based charge-transfer complexes are comprehensively presented.

2. Background and Overview on the Magnetism of Charge-Transfer Complexes

The behavior of magnetic moments is governed by the competition between the thermal agitation and the exchange interaction working to couple the magnetic moments, where the exchange interaction is described as given in the following equation:

$$H = -2J\mathbf{s}_i\mathbf{s}_j \tag{1}$$

where J and $\mathbf{s}_i$ are the coupling constant of the exchange interaction and the spin operator at site i, respectively. Ferromagnetism, in which spins are aligned in parallel, is stabilized as the temperature is lowered enough to overwhelm the thermal agitation when J is positive, whereas negative J gives antiferromagnetism with spins arranged antiparallel to each other. Ferromagnetism is of interest mostly in practical use, as we mentioned in the previous chapter. In contrast, though antiferromagnetic materials, which have no net magnetization due to the antiparallel spin arrangement, are less important from the viewpoint of applications, antiferromagnetism has been attracting physicists due to purely scientific interests. Among them, the quantum mechanical features of antiferromagnetic spin systems have provided important examples for quantum statistical physics,[5,16,17] especially spin systems on low-dimensional frameworks such as 1D or 2D ones.

In designing magnetic materials, therefore, it is important to produce an exchange interaction and interaction network. Here, from this viewpoint, we make a brief perspective on the magnetism of organic charge-transfer complexes having π-electronic structures. Organic charge-transfer complexes consist of electron donors and acceptors, where a π-electron from the HOMO of the donor is transferred to the LUMO of the acceptor. The important structural feature of the organic donors/acceptors is their planar shape, so that the π-electron wave functions that protrude from the molecular plane can easily interact with the wave function of the adjacent molecules. In consequence, the face-to-face molecular configuration, which is stabilized through the intermolecular interaction associated with the overlap of the π-orbitals, gives the molecular stacking arrangements resulting in the formation of a 1D or 2D lattice. Figure 1 shows a schematic model of a 1D molecular arrangement, which is characterized by one π-electron for each HOMO/LUMO state of the donor/acceptor (half-filled state) for simplicity. From the physics viewpoint, the electronic structure of the molecular arrangement is explained in terms of a 1D electronic system with the transfer integral t and the on-site Coulomb repulsion

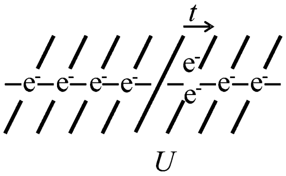

Figure 1. Schematic model of a 1D electronic system comprising the stacking of planar organic molecules where each molecule has a half-filled state except the molecules related to the electron-transfer process. The transfer integral and the on-site Coulomb interaction are denoted by t and U, respectively. The hopping of an electron requires the energy elevation of U.

U between two electrons, the latter of which works when these two electrons are on the same molecule. The transfer integral t is defined for the intermolecular interaction as given by the following equation:

$$t = \int \psi_i^*(x) H_0 \psi_{i+1}(x)\, dx \qquad (2)$$

where H_0 is the Hamiltonian for the one-electron term, and $\psi_i(x)$ is the wave function for molecular site i. The on-site Coulomb interaction U is roughly described in terms of the dielectric constant ϵ and the distance between two electrons r as expressed by

$$U = e^2/\epsilon r \qquad (3)$$

where r is scaled to the size of the molecule on which the two electrons are staying. The expression of the electron motion is given in the following Hubbard Hamiltonian:

$$H = t\sum_{i,\sigma}(c^+_{i,\sigma}c_{i-1,\sigma} + c^+_{i-1,\sigma}c_{i,\sigma}) + U\sum_i n_{i\uparrow}n_{i\downarrow} \qquad (4)$$

where $c^+_{i,\sigma}$ and $c_{i,\sigma}$ are the creation and annihilation operators, respectively, for the electron on molecule i having σ (= ↑ or ↓) spin, and $n_{i,\sigma} \equiv c^+_{i,\sigma}c_{i,\sigma}$ is the number operator of this electron. The first term with the transfer integral that works to hop an electron from molecule i to the neighboring molecule $i - 1$ gives the electrons a mobile feature, while the on-site Coulomb interaction in the second term makes it suppressed. Consequently, the electronic structure of the system is governed by the competition between t and U, which varies from metallic to insulating states depending on the ratio of t/U. Namely, the increase in the ratio favors metallic states, whereas the decrease stabilizes insulating states.

The important roles of these two parameters in the electronic structures can be easily seen on the basis of the combination between the molecular orbital scheme and the valence bond scheme. Figure 2 explains the change in the electronic structures depending on the ratio t/U in relation to these two schemes for a dimer model of acceptor molecules having one electron in their LUMO. In the valence bond scheme with a large U, where an electron is localized on each donor molecule, the hopping of an electron from one molecule to the other requires the energy of U. Therefore, each acceptor in the ground-state possesses one localized electron with a magnetic moment, which is well stabilized by the large excitation energy of U. On the other hand, the molecular orbital regime with large transfer integral t gives a delocalized electronic structure, where two electrons are well delocalized in the dimer unit, resulting in the disappearance of net magnetic moments due to the antiparallel coupling of the spins of the two electrons occupying the same molecular orbital. The intermediate region between the valence bond limit and the molecular orbital limit is described in terms of the two parameters t and U. The ground state of the valence bond scheme is split into two states due to the perturbation of t, where the energy splitting is given by $2t^2/U$. The competition between t and U gives any electronic structure ranging between the two limiting cases in actual organic molecules. The concept of the electronic structures obtained on the basis of the dimer model can be generalized to bulk solids of organic charge-transfer complexes. The valence bond limit $t/U \to 0$ corresponds to the insulating state with localized magnetic moments, which is called a Mott insulator in the solid-state physics language, whereas the molecular orbital limit $t/U \to \infty$ gives a metallic state with the absence of localized magnetic moments. The interesting feature is the presence of the boundary between the insulator state and the metallic state, which is called the Mott–Hubbard boundary. A change of temperature or pressure, which modifies the transfer integral as an intermolecular-distance-sensitive parameter, can make organic complexes pass from the metallic state to the insulating state, resulting in the metal–insulator transition (Mott transition).

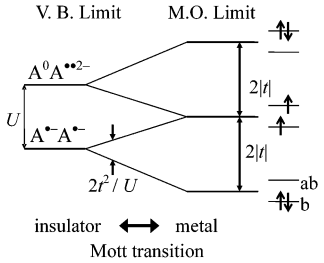

Figure 2. Schematic model of the electronic state of a dimerized acceptor unit AA, which can be generalized to the electronic structure of a bulk system. V.B. Limit and M.O. Limit denote the valence bond limit and the molecular orbital limit, respectively. The transfer integral and the on-site Coulomb interaction are given as t and U, respectively, while b and ab represent the bonding and antibonding molecular orbitals, respectively, in the molecular orbital scheme. In the case of the donor system, the equivalent model is given by replacing electrons with holes.

The strategies for the development of organic complex-based molecular magnets are made on the basis of the scheme with t and U, which are categorized into four classes as shown in Figure 3. In the case of small t/U in the first category, localized magnetic moments are generated on organic molecules which form a low-dimensional magnetic lattice such as a 1D or 2D lattice. The overlap of wave functions between electrons on the adjacent molecules makes an antiparallel spin arrangement, giving an antiferromagnetic interaction with the strength of $J \approx t^2/U$. Moreover, organic molecules consisting of light elements such as C, H, or S have small spin–orbit interactions, so that the magnetic anisotropy whose main origin is eventually the

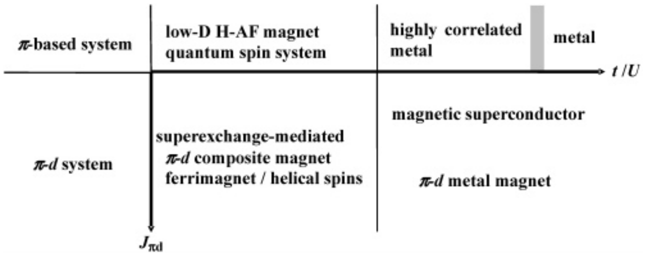

Figure 3. Overview of magnetism appearing in charge-transfer complexes, depending on transfer integral t, on-site Coulomb interaction U, and π−d interaction $J_{\pi d}$. H-AF is the abbreviation of Heisenberg antiferromagnet.

dipole−dipole interaction is considerably small. Consequently, the complexes in this case are characterized basically as low-dimensional Heisenberg antiferromagnetic systems with the features of quantum spins ($s = {}^1/_2$), where the exchange interaction is isotropic, as described in eq 1.

The second category is the case with the intermediate strength of t/U in the vicinity of the Mott−Hubbard boundary, where the features of the metallic state and the insulator state coexist as highly electron-correlated metal. We can realize the coexistence of localized magnetic moments and metallic electron transport. The correlation between magnetism and electron transport provides attractive contemporary topics in this regime.

In the insulating regime (small t/U), incorporating foreign magnetic species into charge-transfer complexes results in magnetic charge-transfer complexes, and these are classified as the third category. The introduction of magnetic ions having d- or f-electrons as a counterpart to an organic donor or acceptor is employed for the development of organic complex-based magnets. In one case of this category in the Mott insulator regime, the localized spins of the π-electrons interact with those of d- or f-electrons on magnetic anions (or cations). On the basis of the Hubbard Hamiltonian for a pair of a π-donor and a magnetic anion of d-electrons, the exchange interaction $J_{\pi d}$ between π- and d-electrons (π−d interaction) is given as follows:

$$J_{\pi d} = 2t_{\pi d}{}^2\left(\frac{1}{U_\pi} + \frac{1}{U_d}\right) \tag{5}$$

where U_π and U_d are the on-site Coulomb interactions in the π-donor molecule and the d-electron of the magnetic anion, respectively, and $t_{\pi d}$ is the transfer integral between the π-donor molecule and the magnetic anion containing the d-electron. The cooperation between the π-electron spins and the d-(f-)electron spins having different magnetic features brings about unconventional composite magnetic systems, such as ferrimagnetic, weak ferromagnetic, helical magnetic systems, and so on. The band insulator, which has a gap of one-electron origin, has no magnetic moment of π-electrons. Even in this case, the role of the π-electron is very important in producing the exchange interaction, that is, the superexchange interaction. By making intermolecular atomic contacts between the organic donor (acceptor) molecule and the magnetic anion (cation), π-electron-mediated superexchange paths between localized d- or f-electron spins can be produced.

It should be noted here that the employment of f-electrons is not appropriate to design composite magnets, since the small wave function of the f-electron cannot produce an interaction strong enough to operate on the π-electron.

Creating a case with a large t/U gives the fourth category belonging to the metallic state. Since the localized magnetic moments of π-electrons are absent, we need to introduce foreign magnetic species having localized magnetic moments in this case, similar to the third category. Magnetic anions/cations having localized d-electrons can be incorporated into charge-transfer complexes. When the interaction between the π-electron and the d-electron (π−d interaction) is weak, these two kinds of electrons behave independently. Therefore, even superconductivity can happen in the π-electron system, while the d-electron spins undergo a magnetic phase transition. In contrast, when the π−d interaction becomes strong, π-conduction carriers work to mediate the exchange interaction between the localized magnetic moments of d-electrons. This is just the molecule version of metal magnets. According to the physics of the s−d interaction in traditional metal magnets such as ferromagnetic iron, unpaired d-electrons, which stay in the inner shell, behave as localized electrons having magnetic moments, while s- and p-electrons are moving freely in the crystal as carriers for the electrical conduction. Thus, d-electrons in a free electron jellium interact with conduction carriers through the s−d interaction expressed by the following equation when a conduction s-electron approaches a d-electron site:

$$-2J_{sd}\delta(\mathbf{r})\mathbf{s}\cdot\mathbf{S} \tag{6}$$

Here, **s** and **S** are the spin operators for a conduction electron and a localized d-electron, respectively, $\delta(\mathbf{r})$ is the δ function, J_{sd} is the coupling constant for the exchange interaction between a conduction s-electron and a localized d-electron, and **r** is the distance between them. In a crystal where this type of interaction is present, the conduction carriers mediate the interaction between localized magnetic moments of d-electrons, giving rise to a long range interaction which is expressed by the following equation:

$$\frac{3N}{16\pi^2}\frac{J_{sd}^2}{E_F}I(\mathbf{R}_{ij})S_{iz}S_{jz} \tag{7}$$

where $\mathbf{R}_{ij}$ is the distance between d-electrons having spins $\mathbf{S}_i$ at site i and $\mathbf{S}_j$ at site j, and E_F is the Fermi energy. $I(\mathbf{R}_{ij})$ is the decaying function of $\mathbf{R}_{ij}$ with a spatially oscillatory behavior, which depends on the Fermi wavenumber k_F, as given by

$$I(\mathbf{R}_{ij}) = -\frac{16\pi k_F^3}{(2k_F\mathbf{R}_{ij})^4}(2k_F\mathbf{R}_{ij}\cos 2k_F\mathbf{R}_{ij} - \sin 2k_F\mathbf{R}_{ij}) \tag{8}$$

The exchange interaction between localized magnetic moments in a metallic medium described in eq 7 is called the Rudermann–Kittel–Kasuya–Yoshida interaction (RKKY interaction), which is the origin of strong ferromagnetism emerging in transition metals such as iron.

It has strategic importance in developing molecular systems having magnetic interactions similar to the s–d interaction in realizing molecular versions of metal magnets. Moreover, this will give new aspects on the phenomena related to the interplay between conduction carriers and localized magnetic moments. Recently, a large variety of organic metals and superconductors have been developed on the basis of organic charge-transfer complexes, where their interesting novel properties have been uncovered. In such organic conductors, the overlap of π-electron wave functions between adjacent molecules gives a small kinetic energy (transfer integral) ranging from 0.1 to 1 eV. Therefore, π-electrons having small kinetic energy play a role in the electron transport process, different from the case of traditional inorganic metals consisting of s- and p-electrons having a large kinetic energy of several electronvolts. In other words, organic conductors are characterized as highly correlated electron systems where the kinetic energy of π-electrons is smaller than or comparable to the on-site Coulomb interaction. Moreover, one of the important features specific to organic complex crystals is the low-dimensionality of their lattices, such as 1D or 2D. Consequently, organic conductors are subjected to electronic instabilities inherent to their low-dimensional electronic structures, resulting in the appearance of insulating states at low temperatures such as charge density wave (CDW) and spin density wave (SDW) states and change ordering. The incorporated d-electron spins in such low-dimensional π-electron conducting systems in addition to the strong electron correlation effect are expected to bring about unconventional features in molecular magnetic conductors, that have never been observed in traditional metal magnets.

There are a large variety of donor molecules in the TTF family, which have been developed in searching for good electrical conducting molecular materials, with high T_c organic superconductors as the ultimate object. By incorporating anions or acceptors into charge-transfer complexes, these TTF-type donors produce a huge number of complexes extending from insulator to metal to superconductor. On the basis of the results in the materials science of TTF-type complexes, we can expect to produce various types of molecular magnets belonging to the categories mentioned above. In the present review article, we discuss the features of magnetic charge-transfer complexes classified into these four categories with important examples in the TTF family, which have been found so far. Figure 4 presents the donor molecules in the TTF family that we discuss in the review.

Sections 3–6 deal with pure π-based magnets in the first category, magnets situated in the metal–insulator boundary in the second category, π–d composite magnets in the third category, and conducting π–d magnets, respectively.

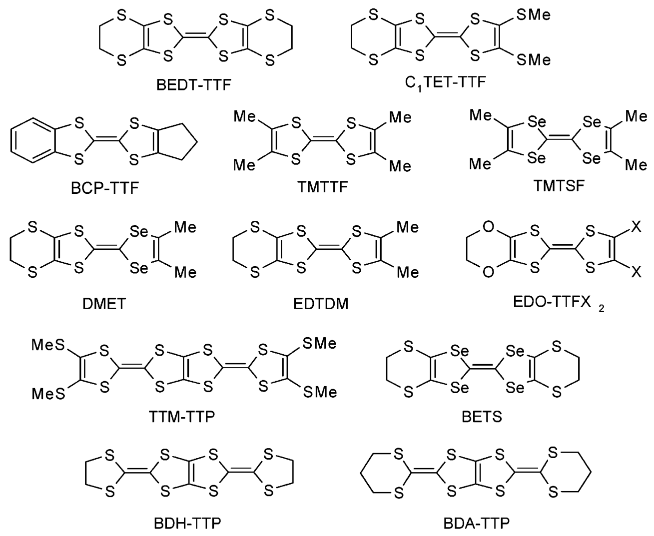

Figure 4. Molecular structure of TTF donors: BEDT-TTF, C_1TET-TTF, BCP-TTF, TMTTF, TMTSF, DMET, EDTDM, EDO-TTFX_2 (X = Br, I), TTM-TTP, BETS, BDH-TTP, and BDA-TTP are the abbreviations of bis(ethylenedithio)tetrathiafulvalene, 4,5-bis(methylthio)-4′,5′-ethylenedithiotetrathiafulvalene, benzocyclopentatetrathiafulvalene, tetramethyltetrathiafulvalene, tetramethyltetraselenafulvalene, 4,5-dimethyl-4′,5′-ethylenedithio-1′,3′-dithia-1,3-diselenafulvalene, 4,5-dimethyl-4′,5′-ethylenedithiotetrathiafulvalene, 4,5-dibromo (or diiodo) -4′,5′-ethylenedioxotetrathiafulvalene, 2,5-bis(4,5-bis(methylthio)-1,3-dithiol-2-ylidene)-1,3,4,6-tetrathiapentalene, bis(ethylenedithio)tetraselenafulvalene, 2,5-bis(1,3-dithiolan-2-ylidene)-1,3,4,6-tetrathiapentalene, and 2,5-bis(1,3-dithian-2-ylidene)-1,3,4,6,-tetrathiapentalene, respectively.

3. π-Based Magnets

TTF-based charge-transfer complexes belonging to the first category possess localized spins of π-electrons in the Mott insulator regime, with the magnetism being featured with localized spin systems. The low-dimensional structures of the complexes conduce to low-dimensionality in their magnetic lattices. Therefore, the magnetic moments of π-electrons ($s = ^1/_2$) on organic molecules are arranged as low-dimensional Heisenberg antiferromagnets with the nature of quantum spins, taking into account the absence of strong magnetic anisotropy due to the spin–orbit interaction. Here, we discuss two kinds of magnetic systems classified as 2D antiferromagnetic systems [β'-(BEDT-TTF)$_2$X (X = ICl_2, $AuCl_2$)[27,28] and (C_1TET-TTF)$_2$Br[29]] and spin Peierls magnets [α'-(BEDT-TTF)$_2$Ag(CN)$_2$[30] and (TMTTF)$_2$X (X = PF_6, AsF_6)[31,32]].

3.1. Quasi-2-Dimensional Heisenberg Antiferromagnets

Isostructural donor–anion sandwich systems β'-(BEDT-TTF)$_2$X (X = ICl_2, $AuCl_2$)[33–37]consisting of dimerized BEDT-TTF donor units are typical examples of quasi-2D Heisenberg antiferromagnets, where each dimer has a localized magnetic moment ($s = ^1/_2$), as summarized in ref 2. According to extended Hückel band calculations,[38] intermolecular side-by-side and face-to-face S···S atomic contacts between BEDT-TTF dimers constitute strong (J_b) and weak exchange (J_c) interactions along the b- and

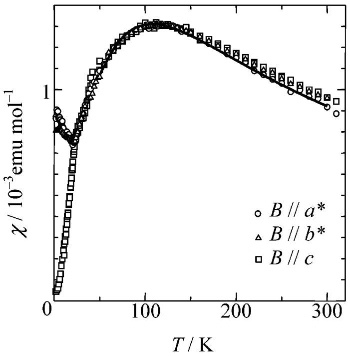

Figure 5. Temperature dependence of the susceptibility of β'-(BEDT-TTF)$_2$ICl$_2$ in the field parallel to the three crystallographic axes. A solid line denotes the best fitting for the 2D square lattice Heisenberg antiferromagnet model.

c-axes on a donor sheet, respectively. The electrical resistivity behaves as a semiconductor with a large activation energy $E_A \approx 0.12$ eV for both ICl$_2^-$ and AuCl$_2^-$ salts, in contradiction to the one-electron picture of band structure. Therefore, the presence of localized spin $s = {}^1\!/_2$ per BEDT-TTF dimer unit proves the feature of Mott insulators. Figure 5 shows the magnetic susceptibility versus temperature plot for the ICl$_2^-$ salt. The temperature-dependent susceptibility of the AuCl$_2^-$ complex and the ICl$_2^-$ complex displays similar trends. Namely, it has a broad peak of short range order around 110 K for both salts, and then an antiferromagnetic transition takes place at $T_N = 22$ and 28 K in the ICl$_2^-$ and AuCl$_2^-$ salts, respectively. The relative strengths of the intra- and interchain exchange interactions on the 2D bc-layers are roughly estimated based on the extended Hückel electronic structure calculation, on the basis of the relation between the transfer integral and the exchange interaction $J \propto t^2$. The estimate gives the ratio of the exchange interactions $J_c/J_b \approx 0.5$, where the numbers of neighboring spins are given to be $z_c = 2$ and $z_b = 2$ from the numbers of transfer integrals connecting neighboring donor dimer units. Theoretical fitting[39] to the observed susceptibility gives a rough estimate of exchange interaction $J = -59$ K for both the ICl$_2^-$ and AuCl$_2^-$ salts, assuming that the magnetic lattices are characterized as 2D square lattices with $J_b = J_c = J$. The difference in the Néel temperatures between the ICl$_2^-$ and AuCl$_2^-$ salts is caused by the contribution of interlayer exchange interaction, since the stability of the 3D long range antiferromagnetic order is sensitive to the interlayer interaction, especially for Heisenberg system. The calculation of interlayer interaction J' based on the Green function method[40] that relates J' with J and T_N gives $J'/J \approx 10^{-4}$ and 10^{-3} for the ICl$_2^-$ and AuCl$_2^-$ salts, respectively. The structural trend that the interlayer distance is shortened by 1.32% as we change anions from larger ICl$_2^-$ to smaller AuCl$_2^-$ is in good agreement with the change in the strengths of the interlayer exchange interactions. One order of magnitude reduction in the interlayer interaction with an only ~1% decrease of the interlayer distance suggests that the short range exchange interaction works between the adjacent donor layers through the nonmagnetic anion layers.

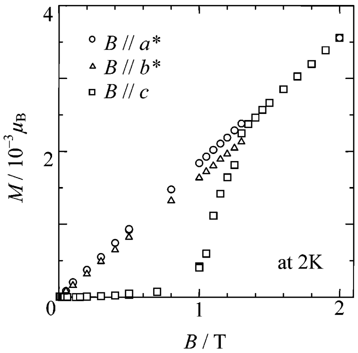

Figure 6. Magnetization curves of β'-(BEDT-TTF)$_2$ICl$_2$ at 2 K in the field parallel to the three crystallographic axes.

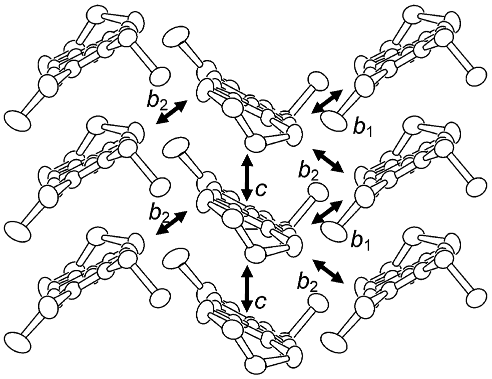

Figure 7. Crystal structure of (C$_1$TET-TTF)$_2$Br and the overlap integrals, which are $b_1 = 5.4$, $b_2 = 4.3$, and $c = 5.8 \times 10^{-3}$ in the bc-plane.

The appearance of anisotropy in the susceptibility and the magnetization curves below T_N show that the easy spin axis is oriented parallel to the c-axis. Figure 6 shows the magnetization curves at 2.0 K for the ICl$_2^-$ salt, which reveal a spin-flop transition taking place at $B_{sf} = 1.1$ T with the magnetic field applied parallel to the c-axis. The spin-flop field B_{sf} is related to the exchange field H_E and the anisotropy field H_A through the relation

$$B_{sf} = \sqrt{H_A(2H_E - H_A)} \tag{9}$$

Using the value of H_E obtained from the exchange interaction J and B_{sf}, the anisotropy field is estimated to be $H_A/H_E \approx 2.0 \times 10^{-5}$. The small anisotropy field is considered to be caused by the dipole–dipole interaction,[41] consistent with the features of the Heisenberg spin system.

3.2. Triangular Antiferromagnet

(C$_1$TET-TTF)$_2$Br is an organic complex characterized in terms of the charge localization and 2D magnetism of localized π-electrons.[29] Figure 7 shows the 2D donor layer structure and the overlap integrals in the bc-plane of (C$_1$TET-TTF)$_2$Br. All the donor molecules, which are uniformly stacked with the same partial charge +0.5, form a 2D zigzag arrangement with a head-to-tail configuration in the interstack direction. The overlap integrals of the donor HOMO calculated by the extended Hückel method[38] are given to be $b_1 = 5.4$, $b_2 = 4.3$, and $c = 5.8 \times 10^{-3}$, which reveal a 2D character with small

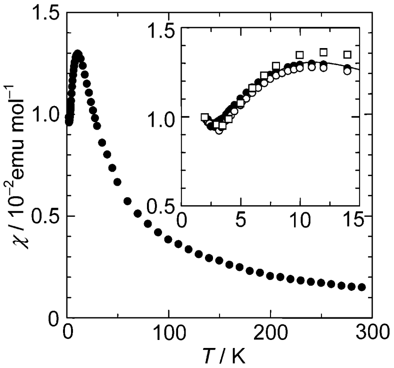

Figure 8. Temperature dependence of the susceptibility in the applied field of $H = 1$ T parallel to the b-axis. The inset shows the temperature dependence of the susceptibility below 30 K in the applied field parallel to the a^*- (filled circles), b- (open circles), and c- (squares) axes. The theoretical fitting (solid line) for the 2D square lattice Heisenberg antiferromagnet model in the temperature range 8−290 K gives an exchange interaction of $J = -6.1$ K, where the 0.5 spin with $s = 1/2$ is allotted to one C_1TET-TTF donor according to the charge distribution. An antiferromagnetic transition is observed at $T_N = 3$ K. (Reprinted with permission from ref 2. Copyright 1997 The Chemical Society of Japan.)

differences in the strengths of the transfer integrals. The band calculation suggests the presence of 2D metallic bands which have narrow bandwidths in the range of 0.4 eV owing to the small overlap integrals. The electrical resistivity is semiconductive with an activation energy of $E_A = 0.2$ eV and the room-temperature resistivity value of $\rho_{RT} = 40\ \Omega$ cm. This result is in disagreement with the band calculation that suggests metallic behavior.

Figure 8 represents the temperature dependence of the susceptibility in an applied field parallel to the b-axis. The susceptibility shows the Curie−Weiss behavior in the high-temperature range, and then it indicates a broad hump of low-dimensional (low-D) antiferromagnetic short range order around 12 K. The susceptibility data in the field parallel to the a^*-, b-, and c-axes are well represented by the Curie−Weiss term with negative Weiss temperature $\Theta = -17.3$ K above 30 K. From the Curie constant, the spin density N is estimated as one localized magnetic moment of $s = 1/2$ per two donors. The detailed susceptibility is exhibited in the inset of Figure 8 in the low-temperature region below 30 K in the applied field parallel to the a^*-, b-, and c-axes. Below 3 K the susceptibility shows an abrupt increase irrespective of field direction. The behavior of the susceptibility and the ESR line width broadening in the low-temperature range suggest the onset of antiferromagnetic order at $T_N = 3$ K. However, it is worth noting the absence of magnetic anisotropy below T_N among the susceptibilities in the field applied parallel to the three independent crystallographic axes. This contradicts the behavior of ordinary antiferromagnets. Moreover, as shown in Figure 9, the magnetization curves in the field parallel to the a^*-, b-, and c-axes at 2 K up to 5 T show a slight concavity with the absence of an apparent spin-flop transition.

Let us now discuss the feature of the charge localization on the donor molecules, which plays an important role in the magnetism. The semiconductive behavior and the presence of localized magnetic moments on the C_1TET-TTF donors suggest features of a Mott insulator generated by the competition between the on-site Coulomb interaction and the transfer integral. Comparison to the reported BEDT-TTF-based Mott insulators[28,42−46] provides an important clue to the electronic structure of the present compound. For instance, α′- and β′-(BEDT-TTF)$_2$X-type Mott insulators have intrinsic half-filled bands due to the strong donor dimerization, where the intradimer transfer integral produces an effective on-site Coulomb interaction in a dimer. The effective on-site Coulomb interaction U_{eff} defined as the on-site Coulomb energy on a dimer unit is given by

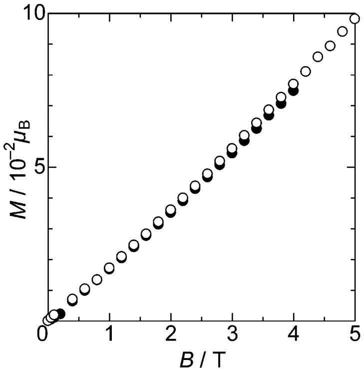

Figure 9. Magnetization curves of $(C_1TET\text{-}TTF)_2Br$ at 2 K.

$$U_{eff} = (U - \sqrt{U^2 + 4t_{intra}^2})/2 + 2|t_{intra}| \approx 2|t_{intra}| \quad (U \gg |t_{intra}|) \quad (10)$$

where U is the on-site Coulomb energy of the individual donor and t_{intra} is the intradimer transfer integral. In these compounds, the effective on-site Coulomb interaction U_{eff} is reduced to $2|t_{intra}|$ because $U \gg |t_{intra}|$. Consequently, the intradimer transfer integral, whose strength is larger than that of the interdimer transfer integral, generates the Mott insulating state, where the magnetic moment is well localized around the region confined in the dimerized unit of BEDT-TTF molecules. On the other hand, the present compound has the intrinsic 3/4-filled band structure due to the uniform donor stacking, indicating that it is not likely to be an ordinary Mott insulator. In this sense, the picture of the donor-dimer-based Mott insulating state seems to fail here; thus, the localized moment is probably widely extended over a unit cell. Accordingly, the features of the electron localization are considered to be situated far from Mott insulators in the ordinary BEDT-TTF complexes, demonstrating that the present compound lies just around the Mott boundary. This less localized nature affects the magnetic behavior in $(C_1TET\text{-}TTF)_2Br$.

The magnetism of the present compounds can be discussed on the basis of the assumption that a 0.5 spin with $s = 1/2$ exists on each donor molecule, although the underlying physics behind it remains to be clarified as a future task. From the extended Hückel calculation, the ratio of the exchange interactions is given to be $J_2/J_1 \sim 0.5$, where the exchange

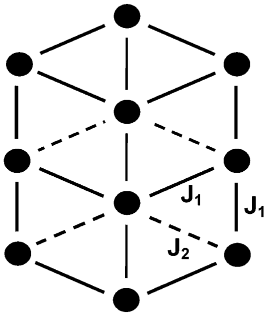

Figure 10. Schematic representation of the triangular magnetic lattice for the C_1TET-TTF layer with antiferromagnetic interactions J_1 and J_2, where the ratio of the interactions is estimated as $J_2/J_1 \sim 0.5$. Solid circles denote the donor molecules, which are regarded as sites having 0.5 spins of $s = {}^1/_2$.

interactions are estimated by $J_1 \approx t_{b_1}{}^2/U \approx t_c{}^2/U$ and $J_2 \approx t_2{}^2/U$ for magnetic neighbors. Therefore, the exchange interaction network is characterized as a distorted triangular lattice with the stronger interaction J_1 and the weaker interaction J_2, as shown in Figure 10. In the case of $J_1 = J_2$, the magnetic system is regarded as a 2D regular triangular lattice antiferromagnet, where the next nearest neighbor connected by J_2 becomes equivalent to the nearest neighbors connected by J_1. In the regular triangular structure consisting of three magnetic sublattices, the antiferromagnetic interaction causes a frustration feature in the spin arrangement, which provides interesting models for classical and quantum spins.[47,48] Actually, in such a case, an antiparallel spin arrangement between two sublattices makes spins on the remaining sublattice frustrated; in other words, the antiparallel coupling of two spins is achieved at the expense of the energy stabilization of the spins which do not participate in the antiparallel spin arrangement. Meanwhile, in the present case having $J_1 > J_2$, the magnetic lattice is expected to be the distorted triangular one. Here, we analyze the susceptibility with a hump at 12 K tentatively by means of the 2D square lattice antiferromagnetic Heisenberg model[39] only with predominant exchange constant J_1 in order to find out the features of the spin frustration. As a result, the susceptibility is well described by the 2D square lattice Heisenberg antiferromagnet model with the exchange energy of $J_1 = -6.1$ K. However, it is worth recalling that the estimated exchange interaction is 1 order of magnitude lower than the exchange interactions of α',β'-(BEDT-TTF)$_2$X[28,49] and θ-(BEDT-TTF)$_2$Cu$_2$(CN)[N(CN)$_2$]$_2$ salts.[50] Actually, the transfer integral between the adjacent dimers in α'- and β'-(BEDT-TTF)$_2$X salts, which have a 2D square antiferromagnetic lattice of the dimerized donors having $s = {}^1/_2$,[28,43−45] is in the same range as the transfer integrals of the present compound despite the large difference in the magnitudes of the exchange interactions. Consequently, the apparent decrease of the estimated exchange interaction in the present compound is proved to be associated with the frustrated spin arrangement through the competition between the antiferromagnetic interactions J_1 and J_2. In relation to the feature of spin frustration, the ordered state below T_N is considered to be characterized as the z_2 vortex state in the triangular antiferromagnetic system with quantum spins,[47,51,52] judging from the absence of magnetic anisotropy shown in Figure 8 in addition to the concave feature of the magnetization curve in Figure 9. The concaved curvature of the magnetization curve in the field applied along the three independent crystallographic directions suggests that the magnetic system becomes more classical upon the elevation of the field.

It is also worth pointing out the importance of the unconventional electronic structure related to the magnetic features; that is, the less localized nature in the electronic structure, as discussed before, may cause the reduction in the strengths of the exchange interactions, in comparison with the ordinary organic Mott insulators that have well localized magnetic moments on donor molecules.

3.3. Spin Peierls Systems

The spin−Peierls transition takes place owing to an instability in $s = {}^1/_2$ 1D Heisenberg antiferromagnetic chains against lattice distortions. The susceptibility of a uniform $s = {}^1/_2$ 1D antiferromagnetic chain has a finite value in the limit of $T \rightarrow 0$, indicating that this spin system is gapless. When the chain is elastically distorted to form dimers, the susceptibility of the resulting alternate chain approaches zero as $T \rightarrow 0$ even though the alternation is weak. This indicates that the dimerization produces an energy gap between the singlet nonmagnetic ground state and the triplet excited states, which stabilizes the exchange energy of the spin system. When this energy gain exceeds the lattice distortion energy, a second-order phase transition takes place, which is called a spin−Peierls transition, in analogy to the Peierls transition of a low-dimensional electronic system. Although the Peierls transition is commonly observed in molecular conductors, the materials which show such a spin−Peierls transition are quite rare. This trend can be explained as follows.[53] The spin−Peierls temperature T_{sP} can be expressed using the BCS theory as

$$k_B T_{sP} = 2.28|J| \exp(-1/\lambda) \tag{11}$$

where J is the (average) intrachain exchange interaction and λ is the spin−phonon coupling constant. As $|J|$ of typical molecular magnets is of the order of 10−100 K, T_{sP} in general corresponds to the temperature where interchain spin−spin coupling cannot be neglected. Consequently, only when the intrachain exchange coupling or spin−phonon coupling is strong enough to dominate the interchain spin−spin coupling, is a spin−Peierls ground state stabilized.

A spin−Peierls transition is not so common in TTF-based charge-transfer complexes. This is because most of the TTF derivatives are originally designed to increase the dimensionality of the π-electronic system, which is unfavorable in forming such a spin−Peierls system. Examples of materials that show a spin−Peierls transition are mainly molecular salts, such as MEM(TCNQ)$_2$ (MEM = *N*-methyl-*N*-ethylmorpholinium),[53,54] (DMeDCNQI)$_2$M (DMeDCNQI = 2,5-dimethyldicyanoquinodiimine, M = Ag, Li),[55,56]

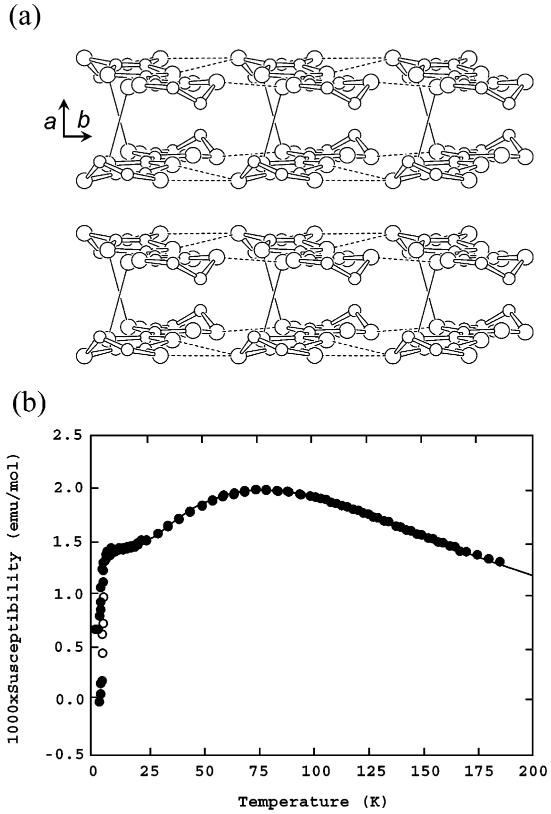

Figure 11. (a) Arrangement of the donor molecules of α′-(BEDT-TTF)$_2$Ag(CN)$_2$. Solid and dashed lines denote intra- and interdimer S···S contacts, respectively, whose distances are shorter than 3.7 Å. (b) Magnetic susceptibility of α′-(BEDT-TTF)$_2$Ag(CN)$_2$ measured at 2 T (open circles) and 5 T (filled circles). The solid line is the 1D Heisenberg antiferromagnet model fitting with $|J| = 59$ K. (Reproduced with permission from ref 30. Copyright 1993 Elsevier.)

TTF[M{S$_2$C$_2$(CF$_3$)$_2$}$_2$] (M = Cu, Au),[57] α′-(BEDT-TTF)$_2$Ag(CN)$_2$,[30] (TMTTF)$_2$X (X = PF$_6$, AsF$_6$),[31,32] and (BCP-TTF)$_2$X (X = PF$_6$, AsF$_6$).[58] These materials are in common made of organic molecules forming 1D columnar stacks, which are sufficiently soft to give rise to a large spin−phonon coupling. As inorganic 1D materials are quite rigid compared to the organic materials, only a few inorganic materials, such as CuGeO$_3$[59] and α-NaV$_2$O$_5$,[60] are known to show a spin−Peierls transition.

In the crystal of α′-(BEDT-TTF)$_2$Ag(CN)$_2$, which is shown in Figure 11a, the donor molecules form a twisted dimer structure having a large difference between intra- and interdimer spacings, which is the origin of the localized character of the π-electron system, as evidenced by the semiconductive behavior of the compound. Due to the presence of side-by-side S···S contacts, these dimers form 1D chains elongated perpendicular to the stacking direction of the donor molecules. Reflecting these structural features, the susceptibility obeys the 1D Heisenberg antiferromagnetic model[61] with $|J| = 59$ K down to ~20 K, as shown in Figure 11b. Below this temperature the susceptibility is somewhat enhanced from the theoretical curve, presumably due to spin fluctuations and the softening of the phonon to which the spins are coupled. At $T_{\rm sP} = 5.8$ K a spin−Peierls transition takes place, below which the susceptibility exponentially decreases as the temperature decreases. This is also evidenced by the presence of a unit-cell doubling along the side-by-side direction, which is observed as X-ray diffuse scattering developing into Bragg peaks at lower temperatures. The possible origin of the spin−Peierls transition of this compound is the weakness of the interchain coupling, which is due to the twisted configuration of donor molecules between the dimers.

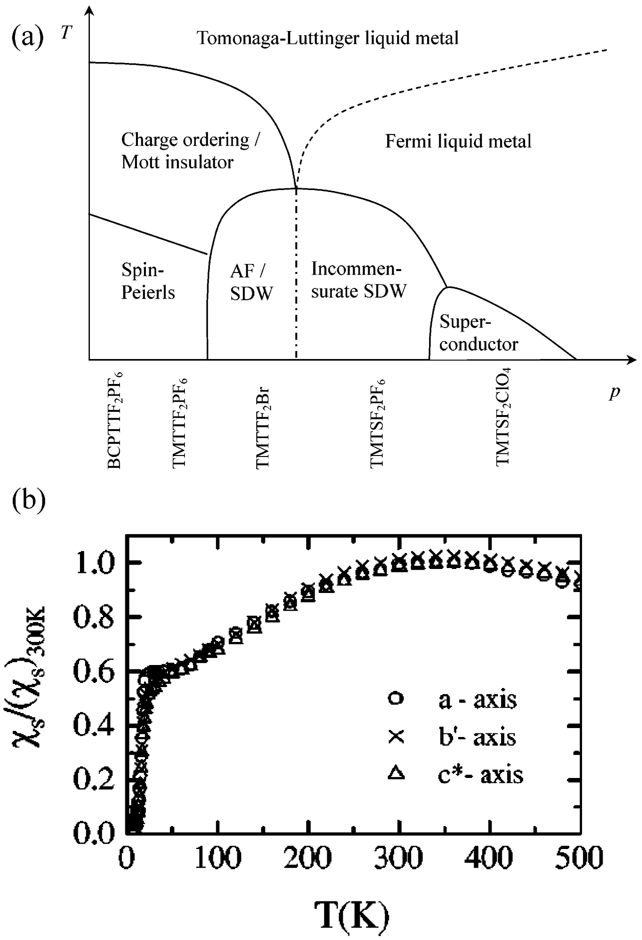

Figure 12. (a) Generalized phase diagram of the TM$_2$X system. For different compounds the ambient pressure position is indicated in the phase diagram. (b) Temperature dependence of the spin susceptibility of (TMTTF)$_2$PF$_6$ in the field along the three crystallographic directions. (Reproduced with permission from ref 31. Copyright 2000 American Physical Society.)

(BCP-TTF)$_2$X and (TMTTF)$_2$X belong to a family of isostructural complexes referred to as the TM$_2$X system, where TM stands for either BCP-TTF, TMTTF, or TMTSF. In this system, the donor molecules, having high planarity, form stacks separated by monovalent anions. The electronic state of the TM$_2$X system can be summarized in the so-called “generic phase diagram”, as illustrated in Figure 12a,[31] where a series of ground states (spin−Peierls, spin−density wave, superconductivity, and metal) appear upon the elevation of chemical pressure (i.e. size of the anion, chalcogen atom of the donor molecule) and/or physical pressure. The application of the pressure mainly affects the transfer integral t between the donor molecules along the stacking direction. Meanwhile, the on-site Coulomb interaction U and nearest-neighbor Coulomb interaction V, which can be controlled mainly by the chalcogen substitution, work to localize the π-electrons. The competition between U, V, and t can produce various electronic states of this TM$_2$X system,[62] including a charge-ordered state where the π-electron system behaves as paramagnetic localized Heisenberg spins interacting with each other through an antiferromagnetic interaction. For the BCP-TTF complexes, the asymmetric donor molecules form head-to-tail dimers within the 1D columns,[63] and the localized character of the π-electrons is more prominent than that of the TMTTF/TMTSF complexes. In this sense these complexes can be located at the low-pressure limit in the generalized phase diagram of the TM$_2$X system.

The susceptibilities of BCP-TTF and TMTTF complexes have been evaluated by the ESR intensity.[31,58] In the high-temperature regime the spin susceptibility obeys the 1D Heisenberg antiferromagnet model with $|J| = 165$, 140, and 210 K for (BCP-TTT)$_2$PF$_6$, (BCP-TTT)$_2$A$_{\mathrm{S}}$F$_6$, and (TMTTF)$_2$PF$_6$, respectively (note that quantity $2J$ in the present article is denoted as J in ref 31). At $T_{\mathrm{sP}} = 37$, 34, and 18 K the spin susceptibility deviates from the 1D Heisenberg antiferromagnet model fit and decreases exponentially below T_{sP}. Especially for (TMTTF)$_2$PF$_6$, as shown in Figure 12b, this exponential decay is observed regardless of the direction of the applied field, suggesting that the ground state is not an antiferromagnetic ordered phase but a nonmagnetic phase. The presence of the lattice modulation is also confirmed by the convergence of the superlattice diffuse scatterings into Bragg spots at the phase transition temperature, which eventually proves the presence of the spin−Peierls transition. Compared to the BEDT-TTF complexes, the TM$_2$X systems are favorable for a spin−Peierls transition when located at the low-pressure limit of the phase diagram probably because of the molecular shape. Both TMTTF and BCP-TTT are highly planar, which ensures the large transfer integral along the $\pi-\pi$ stacking direction leading to the larger intrachain exchange interaction. Besides this, the presence of terminal methyl, trimethylene, or benzo groups also works as a steric hindrance to weaken the interchain coupling.

4. Magnets in the Mott−Hubbard Boundary

TTF-based complexes form a low-D π-electronic state, where the transfer integral and the on-site Coulomb interaction are occasionally competing with each other, resulting in the appearance of a situation of the Mott−Hubbard metal−insulator boundary, as we pointed out in section 2. Especially, for dimerized donor arrangements which are often stabilized in TTF-type complexes, the competing situation is experienced in many cases, since the problem of t/U is reduced to that of $|t_{\mathrm{inter}}|/|t_{\mathrm{intra}}|$ according to eq 10. Indeed, we know several typical cases in the Mott−Hubbard boundary with donors dimerized in (TMTTF)$_2$X.[63−66]

The electron correlation effect, which tends to bring us to the electron localized regime, becomes more significant as the dimensionality is lowered. According to theoretical prediction,[67,68] the electron correlation in 1D electronic systems leads to the duality of the spin−charge separation in the Tomonaga−Luttinger liquid state, which means that metallic conduction and localized spins coexist in a material. Therefore, TTF-based charge-transfer complexes in this regime can be interesting conducting molecular magnets, where electron transport and magnetism interplay. Actually, several complexes belonging to this regime have been found so far, where θ-(BEDT-TTF)$_2$RbZn(SCN)$_4$,[69] (BEDT-TTF)$_2$Br·CH$_2$(OH)CH$_2$OH,[2] (TMTTF)$_2$X (X = Br, PF$_6$),[63−66] (TTM-TTP)I$_3$,[70] and (EDO-TTFBr$_2$)$_3$I$_3$[71] are typical examples. The correlation of electron conduction and localized magnetism can be easily seen by making a resistivity versus susceptibility plot as shown in Figure 13,[71,72] where the former and the latter represent the features of electron transport and localized spins, respectively. In the regime where resistivity and susceptibility are low and small, respectively, metallic features appear as indicated by open circles, whereas high resistivity and high susceptibility bring about a Mott insulating state. The Mott−Hubbard boundary is the regime having low resistivity and high susceptibility. There are interesting examples classified in the Mott−Hubbard boundary among the materials investigated. The first one is (TTM-TTP)I$_3$,[70] which is metallic even though its half-filled electronic state evidently prefers an insulating state. The second one is (EDO-TTFBr$_2$)$_3$I$_3$,[71] which shows most typically the coexistence of a metallic state and a localized magnetic moment just around the Mott−Hubbard boundary. The next two subsections are devoted to these two examples.

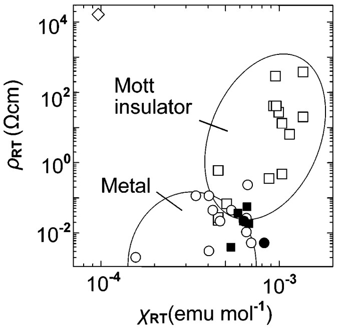

Figure 13. Diagram of the resistivities vs susceptibilities at room temperature for various TTF-based complexes: filled circles, (EDO-TTFBr$_2$)$_3$I$_3$; filled squares, (TMTTF)$_2$X; open squares, Mott insulators; open circles, metals; diamonds, band insulators. (Reproduced with permission from ref 71. Copyright 2003 American Physical Society.)

4.1. Magnetism of the Mott−Hubbard Boundary in the Half-Filled State

Complex (TTM-TTP)I$_3$ forms a completely 1D electronic structure along the c-axis with the ratio of interchain transfer integral to intrachain transfer integral being $t_{\perp}/t_{\parallel} < 0.04$ as large flat-shaped TTM-TTP donor molecules featured with fused TTF molecules tend to be stacked in a face-to-face manner.[70] The band calculation shown in Figure 14 reveals the 1D metallic feature in the electronic state. An interesting point that has to be stressed is that the 1:1 stoichiometry of the donor-to-anion ratio creates a half-filled electronic state; that is, one electron is

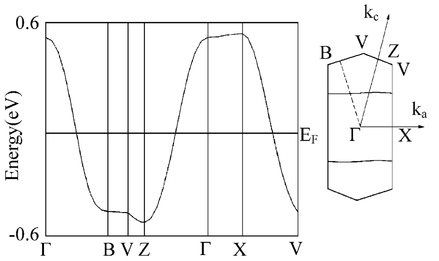

Figure 14. Band structure of (TTM-TTP)I_3. (Reproduced with permission from ref 70. Copyright 1997 American Physical Society.)

transferred to the anion, making the donor HOMO level half-filled. In the one-electron scheme of band theory or the molecular orbital picture, the Fermi energy is placed in the middle of the HOMO band (conduction band). However, as clearly understood based on the valence bond scheme in Figure 2, the on-site Coulomb interaction produces a gap of $U - 4t$, that separates the completely occupied down-spin state and unoccupied up-spin state, stabilizing an insulating state. In other words, when an electron in the donor concerned hops to the adjacent donor site, the upper up-spin state of the latter becomes completely filled, resulting in the generation of a large on-site Coulomb interaction. (The bandwidth in a 1D system is given as $4t$ in place of the level splitting of $2t$ in the dimer case shown in Figure 2.) Therefore, the half-filled state cannot be metallic due to the large electron correlation effect.

On the contrary, the experimental fact is beyond this conjecture. Indeed, the conductivity, whose value is very high with a room-temperature conductivity of 700 S cm^{-1}, shows metallic features down to $T_{MI} \sim 160$ K, below which an insulating phase is stabilized. According to the optical reflection spectra analyzed on the basis of the Hubbard model,[73] the intrachain transfer integral and the on-site Coulomb interaction are estimated as $t_{||} = 0.16$ eV and $U = 0.57$ eV, respectively. The large molecular size of the TTM-TTP donor is responsible for the small U observed, as easily understood from eq 3. Eventually, the bandwidth $4t_{||} = 0.64$ eV slightly overwhelms U, with the 1D metallic state being able to survive down to T_{MI} despite the contribution of the large electron correlation effect. Here, it is important to characterize the metal−insulator transition. A possibility of a charge density wave state is excluded according to the absence of diffuse lines or satellites in the X-ray diffraction data in the insulating phase. The spin susceptibility, which is shown in Figure 15, provides information on the electronic properties in relation to the nature of the MI transition. The susceptibility exhibits a monotonically decreasing trend with a slight slope, approaching a finite value at $T = 0$ K as the temperature is lowered. It is worth noting that no anomaly appears at T_{MI}. This trend in the susceptibility in the whole temperature range can be explained in terms of a 1D Heisenberg antiferromagnet[61] with localized spins $s = {}^1\!/_2$ and an exchange interaction of $J = -640$ K, which is well reproduced from the theoretical estimation ($J \sim 2t^2/U$). This clearly suggests that localized spins exist not only in the insulating state but also in the metallic phase.

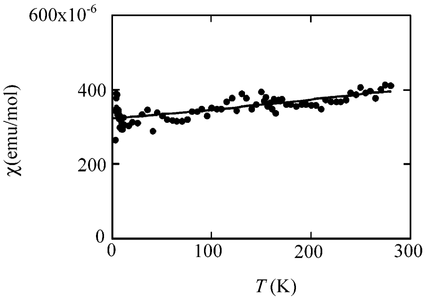

Figure 15. Susceptibility as a function of temperature under a magnetic field of 1 T for (TTM-TTP)I_3. The solid curve represents the 1D Hiesenberg antiferromagnet model. (Reproduced with permission from ref 70. Copyright 1997 American Physical Society.)

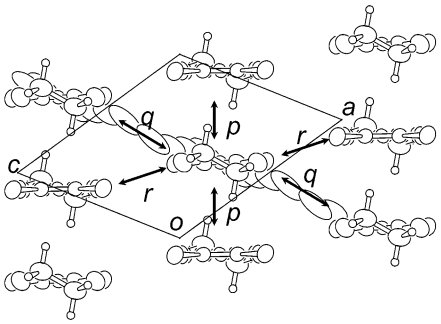

Figure 16. Donor arrangement of (EDO-TTFBr$_2$)$_3$I$_3$ projected on the *ac*-plane. Interdonor transfer integrals are estimated as $p = 3.4 \times 10^{-2}$, $q = -1.1 \times 10^{-2}$, $r = -7.0 \times 10^{-3}$. I_3^- anions are placed above and beneath the donor layer. (Reproduced with permission from ref 71. Copyright 2003 American Physical Society.)

The coexistence of conduction carriers and localized magnetic moments evidences that (TTM-TTP)I_3 is classified in the Tomonaga−Luttinger liquid in the 1D electronic system, where spins and charges are completely separated.[67,68]

The metallic conduction of the present system can be attributed to the thermal excitation across the charge gap. Since U is comparatively small, the charge gap is comparatively small, resulting in apparently metallic conduction at high temperatures. If this explanation is valid, the population of the doubly occupied sites must be of fundamental significance at least in the metallic temperature regime.

4.2. Clear Evidence of Metallic Conduction and Localized Spins

As discussed in the beginning of this chapter, (EDO-TTFBr$_2$)$_3$I$_3$ is situated most typically in the vicinity of the Mott−Hubbard boundary, in which metallic conduction and a localized magnetic moment coexist.[71] (EDO-TTFBr$_2$)$_3$I$_3$ forms a 1D donor column along the $a + c$ direction, in which asymmetric planar-shaped donors are stacked in a head-to-tail fashion, as shown in Figure 16. The donor columns are two-dimensionally arranged in the *ac*-plane, where I_3^- anions are sandwiched between donor layers, making the adjacent donor layers placed apart from each other. From the crystal structure analysis, the elemental analysis, and the Raman data, the valence of EDO-TTFBr$_2$ is estimated at $+{}^1\!/_3$. The charge-transfer rate between donors and anions is

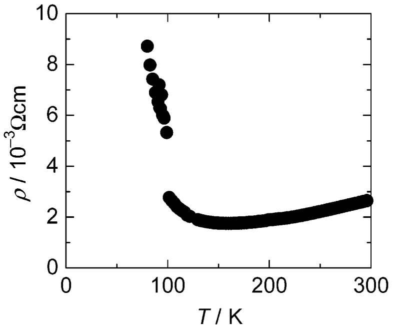

Figure 17. Temperature dependence of the resistivity for (EDO-TTFBr$_2$)$_3$I$_3$. (Reproduced with permission from ref 71. Copyright 2003 American Physical Society.)

demonstrated to be temperature-independent from the Raman data down to 2 K.

According to the extended Hückel calculation, each donor column is characterized by a unique intrachain transfer integral p, which is 4−6 times larger than the interchain transfer integrals q and r, suggesting a quasi-1D electronic nature. The band structure obtained from the tight binding scheme predicts a metallic nature with the presence of a 2D Fermi surface, which suggests the important role of interchain transfer integrals.

The resistivity behaves consistently with the predicted band structure in part, showing metallic resistivity with a room-temperature value of 10^{-2} Ω cm, as exhibited in Figure 17. The resistivity ρ decreases as the temperature is lowered down to about 150 K, and then it shows a semiconductive upsurge with a MI transition taking place at $T_{\mathrm{MI}} \sim$ 100−150 K. In contrast, the magnetic properties are apparently inconsistent with the electron transport properties. Figure 18a shows the temperature dependence of the susceptibility χ. It increases as the temperature is lowered down to ~70 K, and then it shows a steep decrease after a broad maximum around 70 K. The susceptibility changes discontinuously at 15 K, below which it increases. Interestingly, no discontinuous change is observed in the susceptibility at the metal−insulator transition around 100−150 K. The behavior of the susceptibility in the high-temperature range above 15 K is reminiscent of that expected for a 1D Heisenberg antiferromagnetic system of localized spins, which seems to be inconsistent with the metallic features of the conduction carriers. Fitting with the 1D Heisenberg antiferromagnet model[61] gives estimates of the exchange interaction $|J| \sim 62$ K and the localized spin concentration of 0.23 spin/donor. From the transfer integrals, the strength ratio of the interchain to intrachain exchange interaction is estimated at 0.1, which justifies the employment of the 1D Heisenberg antiferromagnet model in the analysis. There is a deviation from the model at high temperatures above ~120 K, which is pronounced as the temperature is elevated. This suggests the inappropriateness of the fitting with the 1D Heisenberg antiferromagnet model in the high-temperature range at least above ~150 K. The estimated spin concentration is less than that expected from the donor/anion composition ratio $^1/_3$. This also implies that the 1D Heisenberg antiferromagnet model does not necessarily represent the behavior of the magnetism. An alternative explanation of the apparent small localized spin concentration is associated with a fractional value of a localized spin, which might come from a trace of an itinerant feature of the electron in the metal−insulator boundary.

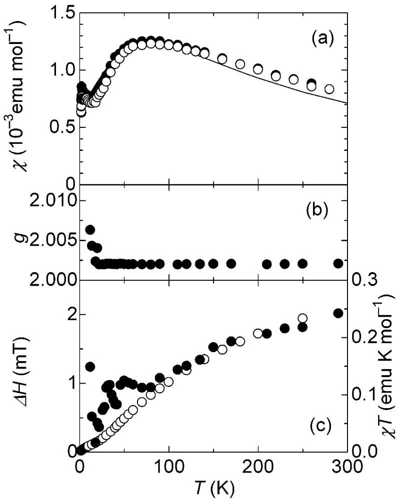

Figure 18. (a) Temperature dependence of the static susceptibility under the magnetic field of 1 T for (EDO-TTFBr$_2$)$_3$I$_3$: open circles, $B \parallel b$-axis; solid circles, $B \parallel a+c$ direction; solid line, 1D Heisenberg antiferromagnet model with $J = -62$ K and 0.23 spins/donor. The steep drops appearing below ~10 K come from an overestimation of the Curie impurities. (b) ESR g-value and (c) line width (filled circles) as a function of temperature for the $B \| a+c$ direction. The product of the temperature T and the susceptibility χ measured in the same direction is also plotted (open circles). (Reproduced with permission from ref 71. Copyright 2003 American Physical Society.)

Eventually, the behavior of the susceptibility evidences the presence of localized magnetic moments in a 1D Heisenberg antiferromagnetic system, whereas the electron transport properties are explained in terms of metallic conduction carriers. In other words, the present electronic system has features of both metallic and localized electrons, which are not compatible according to the conventional theory of electrons. The enhanced deviation of the susceptibility from that expected from the 1D Heisenberg antiferromagnet model in the high-temperature range above about ~150 K proves that the metallic feature is pronounced at the expense of the feature of localized spins in that temperature range.

The ESR spectra include important information on the spin system, which provides a diagnosis in characterizing features between itinerant and localized electrons. As shown in Figure 18c, the line width decreases monotonically as the temperature is lowered, where the temperature dependence is well in accordance with the temperature dependence of the product χT. Such a correlation between the line width and χT is typically observed in low-D antiferromagnets,[74] which is associated with the spin-diffusion process of the localized spin system. Therefore, the ESR spectra observed are suggestive of the feature of localized spins in a low-D framework.

The discontinuous change in the susceptibility at $T_{\mathrm{N}} \sim 15$ K is the consequence of the onset of an antiferromagnetic phase transition. The presence of the transition is also supported by the behavior of the ESR and the magnetization below T_N. The ESR signal abruptly disappears at T_N, suggestive of the onset of an antiferromagnetic transition. The magnetization curves below T_N show a spin–flop anomaly at $B_{sf} \sim 0.5$ T in the field parallel to the *b*-axis. The spin–flop transition behavior indicates that the spin easy axis is oriented parallel to the *b*-axis in the ordered state.

5. *π*–*d* Composite Magnets

π–d composite magnets can be produced by incorporating counteranions having magnetic d-electrons into TTF-type complexes. The interaction between the π-electrons and the d-electrons can be produced through short intermolecular atomic contacts, through which the wave functions overlap between the two components. In insulating materials, the interaction originates from a superexchange interaction, in contrast to the case of metallic materials, which are subjected to conduction–electron-mediated interactions, as discussed in section 2. In developing such π–d composite systems and enhancing their π–d interaction, much effort has been made so far by employing mainly transition metal halides as counteranions,[75–96] leading to a variety of π–d composite magnets.

In enhancing the interaction through the wave function overlap, there are two important issues to be taken into consideration. First, the d-electrons of the counteranion should be sufficiently delocalized onto the ligand atoms. Second, there should be close contacts between the ligand of the anion and the donor molecule. These two can be good guiding principles in selecting donor and anion molecules in designing π–d systems. Based on these principles, the transition metal halides have been the popular choice as magnetic anions and the trend in the strengths of the exchange interactions of 3d transition metal halides MX_2 (M = Mn, Fe, Co, Ni, Cu; X = F, Cl, Br) provides us useful hints for understanding their magnetic behavior. Figure 19 presents the transition metal species dependence of the Néel temperatures, which roughly represent the strength of the exchange interaction, in the 3d transition metal halides.[97] According to the trend shown in Figure 19a, the magnetic interaction between d-electrons becomes weaker in the order F > Cl > Br > I except for copper halides, where it becomes strengthened considerably. When we focus on bromides, the interaction is elevated as the number of d-electrons increases, as exhibited in Figure 19b. Especially, $CuBr_2$ has a remarkably large exchange interaction between the localized spins, due to the spin polarization largely extended onto ligand bromine atoms, which is caused by the delocalized feature of d-electrons on the copper atom, suggesting the advantage of using $CuBr_4^{2-}$ as a counteranion. Actually, the electronic structure calculation suggests the extended electronic state of $CuBr_4^{2-}$. From the practical aspects in sample preparation, however, this anion exists in the solution only under the high concentration of the Br^-;[98] hence, the Br^- salt tends to be stabilized instead of the desired $CuBr_4^{2-}$ salt. This situation makes the preparation of $CuBr_4^-$ salts rather difficult except for the exceptional cases of (TTM-TTF)$CuBr_4$[83] and (BEDT-TTF)$_3CuBr_4$.[76,85,86,91,93] On the other hand, FeX_4^- ions are relatively stable and are easily handled in the preparation of complexes.

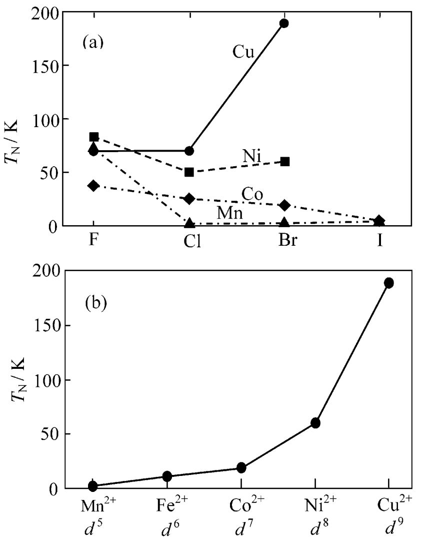

Figure 19. Transition metal species dependence of the Néel temperature T_N in 3d transition metal halides MX_2: (a) T_N as a function of halogen species X for M = Mn, Co, Ni, and Cu; (b) T_N vs number of d-electrons for transition metal bromides.

Theoretical estimations of the π–d interaction have been made on the basis of the spin restricted extended Hückel molecular orbital calculations, which are imperatively useful in designing π–d composite magnets.[99] Figure 20 presents the calculated contributions of the π–d interaction and those of the direct d–d interactions to the Weiss temperatures in the π–d composite magnets having been investigated so far. From the results of the calculations, there are two regimes in the contribution of the π–d interactions. One is the regime where the π–d interaction overwhelms the direct d–d interaction, whereas it contributes less importantly in the other regime. These two regimes exist in both insulating and metallic materials. The calculated strengths of the π–d interactions can be understood roughly on the basis of the guiding principle mentioned above.

The following two subsections are devoted to π-electron-mediated superexchange interaction systems and π–d composite magnets with interesting examples.

5.1. *π*-Electron-Mediated Superexchange Interaction Systems

In the band insulator regime, where the π-electrons have no localized magnetic moments, the introduced localized spins of the d-electrons in the counteranions can be coupled to each other through the π-electron-mediated superexchange paths when short intermolecular atomic contacts are present between the donor and the anion. Therefore, intentional designing of a molecular arrangement with the cooperation of donor π-electrons is expected to result in a large

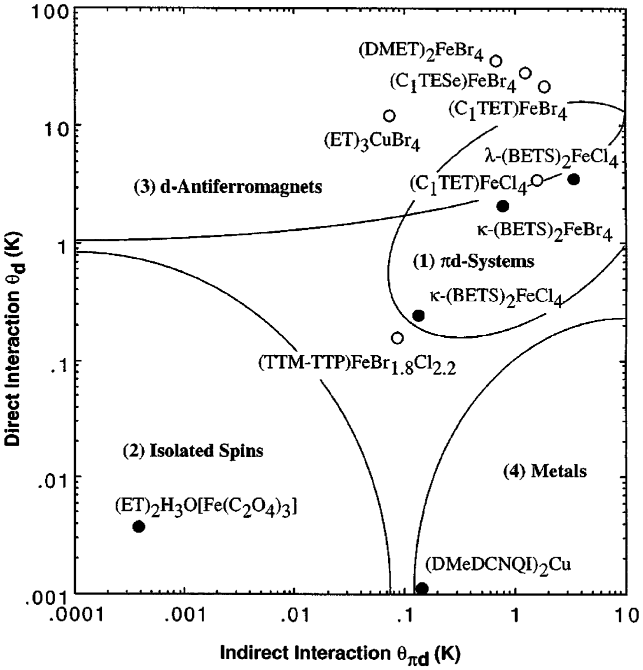

Figure 20. Calculated contributions of the direct d−d exchange interaction and the indirect π-d interaction to the Weiss temperatures for the π−d composite magnets having ever been investigated. The closed circles designate metallic compounds at low temperatures. ET is the abbreviation for BEDT-TTF. (Reproduced with permission from ref 99. Copyright 2002 The Physical Society of Japan.)

variety of d-electron-based molecular magnets having different dimensionality and magnetic features such as antiferromagnetism, ferromagnetism, weak ferromagnetism, and so forth. There are many examples of π-electron-mediated superexchange interaction systems: (TMTSF)FeCl$_4$, (TMTTF)FeCl$_4$,[75] (BEDT-TTF)$_3$(MnCl$_4$)$_2$,[78] (BEDT-TTF)$_4$Cu(C$_2$O$_4$)$_2$,[84] (C$_1$TET-TTF)CuBr$_4$,[83] (C$_1$TET-TTF)FeX$_4$ (X = Cl, Br),[100−102] and so forth. Here, we discuss the magnetism of (C$_1$-TET-TTF)FeX$_4$ (X = Cl, Br), which are characterized by a triangle-based ladder lattice with weak ferromagnetism.

(C$_1$TET-TTF)FeX$_4$ (X = Cl, Br) are interesting examples of a spin ladder system, as shown in Figure 21. They are composed of Fe^{3+} zigzag chains mediated by the direct anion−anion contacts (Fe−X···X−Fe) and C$_1$TET-TTF donor dimers. In an anion chain, every two Fe^{3+} sites are coupled by anion−donor−anion contacts (Fe−X···D···X−Fe), where D represents a C$_1$TET-TTF donor. The direct anion−anion contact and the indirect anion−donor−anion contact work to give antiferromagnetic superexchange paths J_1 and J_2, respectively, resulting in the formation of a triangle-based spin-ladder system where J_1 and J_2 correspond to the rung and leg of a ladder, as shown in Figure 22a. In addition to these two interactions, two adjacent chains are coupled by a weak antiferromagnetic interaction J_3 mediated by a donor dimer (Fe−X···(D$_2$)···X−Fe).

Figure 23a shows the temperature dependence of the susceptibility for X = Br. The susceptibility obeys the Curie−Weiss law with an antiferromagnetic Weiss temperature of $\Theta = -18$ K. A broad hump appearing around 10 K is suggestive of short range order, for which low-dimensionality in the magnetic structure is responsible. The susceptibility shows an antiferromagnetic transition at $T_N = 4.2$ K, below which the spin easy axis becomes oriented in the a-axis direction. The peak at T_N, which is accompanied by field dependent susceptibility behavior in the b-axis direction, suggests weak ferromagnetism. The weak ferromagnetic feature is clearly seen in the magnetization curves shown in Figure 23b. The magnetization curve has a spin−flop transition at $B_{sf} = 2.3$ T in the a-axis direction, while the b-axis magnetization gives an additional magnetization above weak ferromagnetic transition field $B_{wf} = 2.3$ T, which is fortuitously the same as the spin−flop field. The additional magnetization originates from the spin-canting-induced weak ferromagnetism, as shown in Figure 22b. The weak ferromagnetic component generated in sublattices a and b of a ladder is compensated by that generated in sublattices c and d of the adjacent ladder below B_{wf}. From the difference between the straight lines fitted to the magnetization curves well below and above B_{wf}, the weak ferromagnetic magnetization is estimated as $\Delta M_{wf} \sim 0.21\mu_B$, which corresponds to a canting angle of 3.8°. The weak ferromagnetic transition at B_{wf} can be explained in terms of the rotation of the weak ferromagnetic moments between the adjacent ladders in the manner that a net magnetization is generated at the expense of the energy gain of J_3 in the direction of the applied field in the high field state, as shown in Figure 22b.

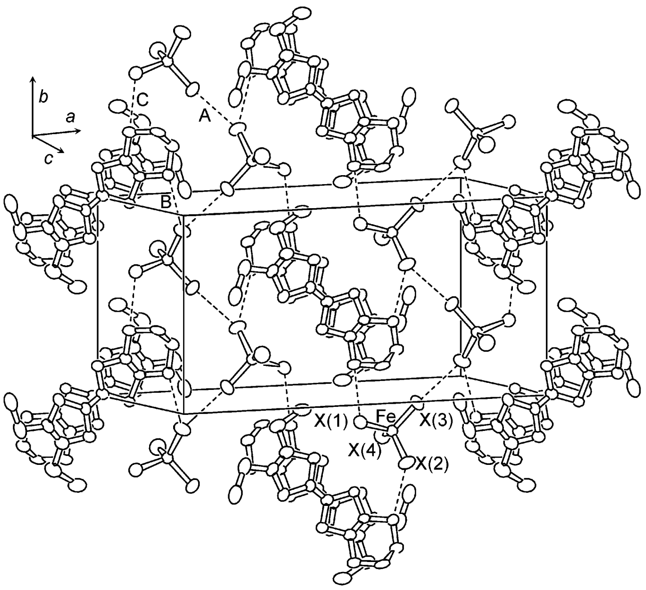

Figure 21. Crystal structure of (C$_1$TET-TTF)FeX$_4$ (X = Cl, Br). There are close atomic contacts between two halogen atoms (A) of adjacent FeX$_4^-$ anions and those of halogen−sulfur atoms (B, C) between FeX$_4^-$ and the C$_1$TET-TTF donor.

The spin-canting-induced weak ferromagnetism is considered to be associated with the Dzyaloshinski−Moriya interaction or the difference in the crystal field anisotropy between two kinds of FeX$_4^-$ sites. Indeed, the Dzyaloshinski−Moriya interaction can possibly be the origin of the weak ferromagnetism, since the inversion center is absent between the adjoining two anion spin sites. Another possible

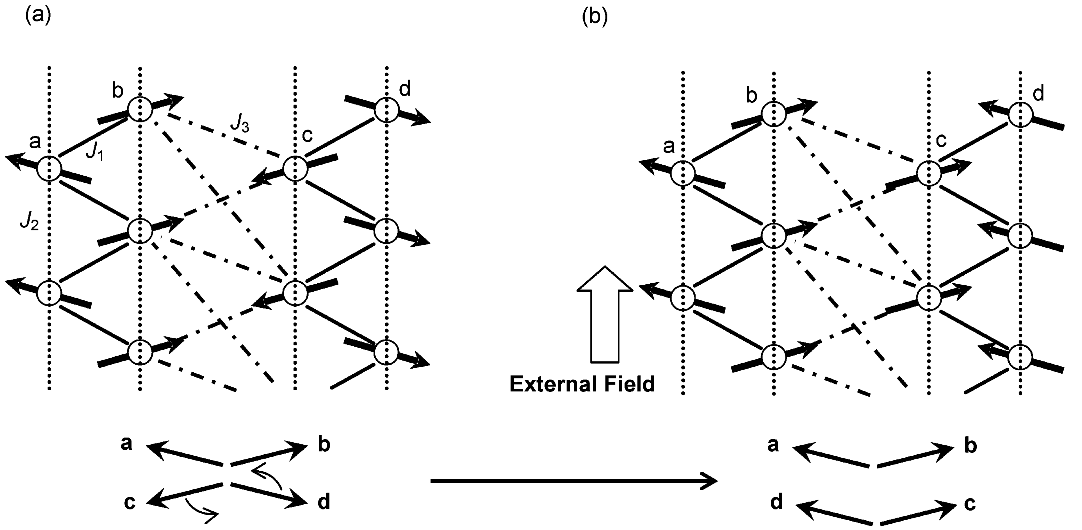

Figure 22. (a) Schematic model of the exchange interaction path network for triangle-based spin ladder system (C_1TET-TTF)FeX_4 (X = Cl, Br). Solid, dotted, and dot−dash lines represent superexchange paths for J_1, J_2, and J_3, respectively, which correspond to the paths Fe−X···X−Fe, Fe−X···D···X−Fe, and Fe−X···(D_2)···X−Fe, where D is donor. a, b, c, and d denote sublattices constituting the unit cell of the magnetic lattice. Arrows represent the spin arrangement in the antiferromagnetic ordered state. The spin structure shown in part a corresponds to the ordered state below the weak ferromagnetic transition B_{wf}. (b) The ordered state above B_{wf}. (Reproduced with permission from ref 100. Copyright 1999 Taylor & Francis, Inc., http://www.routledge-ny.com.)

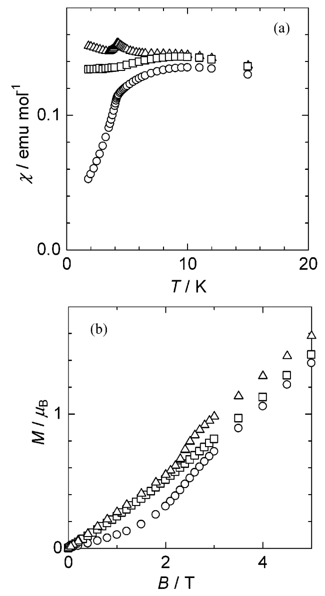

Figure 23. Temperature dependence of the susceptibility at $B = 1$ T (a) and the magnetization curves at 2 K (b) for (C_1TET-TTF)$FeBr_4$ in the field parallel to the *a*-, *b*-, and *c*-axes, which are represented by circles, triangles, and squares, respectively. (Reproduced with permission from ref 100. Copyright 1999 Taylor & Francis, Inc., http://www.routledge-ny.com.)

candidate for this type of behavior is the single ion anisotropy. The tetrahedral $FeBr_4^-$ anion is uniaxially distorted with respect to the elongated Fe−X(1) bond (see Figure 21 for the structure of the $FeBr_4^-$ anion). There are two kinds of $FeBr_4^-$ sites whose distortion axes have a mutual angle of 30°. Therefore, the difference in the anisotropy axes of single ion anisotropy is also responsible for the weak ferromagnetism. The observed small canting angle, which is an order of magnitude smaller than the mutual angle of the anisotropy axes, is the consequence of the competition between the antiferromagnetic exchange interactions and the magnetic anisotropy.

The strengths of the exchange interactions can be estimated from the parameters experimentally obtained on the basis of molecular field treatment. In a spin ladder, the molecular fields associated with J_1 and J_2 can be related to the Néel temperature and the Weiss temperature as shown in the following equations:

$$\Theta = \frac{N(g\mu_B)^2 S(S+1)}{6k_B}\frac{1}{2}(A+\Gamma) \tag{12}$$

$$-\frac{\Theta}{T} = \frac{A+\Gamma}{A-\Gamma} \tag{13}$$

$$A = \frac{2z_1J_1}{(N/2)(g\mu_B)^2}, \quad \Gamma = \frac{2z_2J_2}{(N/2)(g\mu_B)^2} \tag{14}$$

where $z_1 = 2$ and $z_2 = 2$ are the numbers of the neighboring spins connected by J_1 and J_2, respectively. N is the number of the spin sites in a ladder. For the estimation of J_1 and J_2, we employed the value of the short range order hump temperature as the representative of T_N, because the discussion is based on the molecular field framework. The estimation gives $J_1 \sim -1.76$ K and $J_2 \sim -0.5$ K. The interladder interaction J_3 is estimated from the difference of energies between the low field state (E_l) and the high field state (E_h) at B_{wf}, which correspond to the states shown in parts a and b, respectively, of Figure 22 and are given in the following equations:

$$E_l = 2J_1SS + 2J_2SS - 3J_3SS \tag{15}$$

$$E_h = 2J_1SS + 2J_2SS + 3J_3SS \tag{16}$$

where the number of neighbors connected by J_3 is

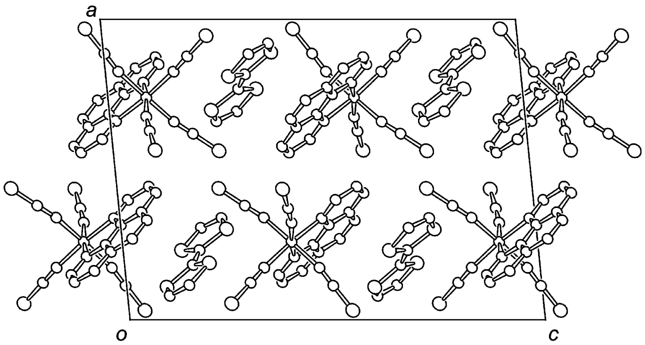

Figure 24. Crystal structure of (TTF)[Cr(NCS)$_4$(phen)] viewed along the (010) direction. (Reproduced with permission from ref 105. Copyright 2000 Royal Society of Chemistry.)

$z_3 = 3$. Then the energy difference is equated to the energy gain produced by the weak ferromagnetic transition as given by

$$\Delta M_{\mathrm{wf}} B_{\mathrm{wf}} = E_{\mathrm{h}} - E_{\mathrm{l}} = 6 J_3 SS \tag{17}$$

Thus, the estimation gives $J_3 \sim 9 \times 10^{-3}$ K, which is about 1 order of magnitude smaller than J_1 and J_2, proving that the triangle-based spin ladder structure is well defined.

From the above molecular field treatment, the ratio of J_2/J_1 is estimated at 0.28. According to theory with the triangle-based ladder system of classical spins,[103] a collinear antiferromagnetic state is stabilized for $J_1/J_2 < 0.25$, while a spiral state appears above that ratio. This suggests an apparent inconsistency in the case of X = Br. The role of the interladder interaction J_3 [($\sim 6 \times 10^{-3}$)J_1] is found to be crucial in the stabilization of the antiferromagnetic state observed.

5.2. π–d Composite Localized Spin Magnets

In the Mott insulating regime of the π-electrons, the localized spins of the donor π-electrons can interact with the localized spins of the d-electrons of the counteranions through π–d-superexchange interaction paths. In this case, the two kinds of spins, which have different magnetic features such as differences in spin values, anisotropies, and so on, cooperate in giving π–d composite magnets. Indeed, the donor π-electron has $s = {}^1/_2$ with weak magnetic anisotropy, while the d-electron has various spin values from ${}^1/_2$ to ${}^5/_2$, with the magnetic anisotropy being changed in a wide range from an isotropic Heisenberg feature to an anisotropic Ising or XY one depending on the transition metal species. Therefore, various types of magnetism, such as ferrimagnetism, weak ferromagnetism, helical spins, and so on, can be brought about, although intentional material designing of this class of materials has not been carried out well so far. Here, we discuss interesting examples with the coexistence of ferrimagnetism and weak ferromagnetism.

Charge-transfer complexes of TTF, TMTTF, BEDT-TTF, and TMTSF with [M(isoq)$_2$(NCS)$_4$]$^-$ (isoq = isoquinoline (C$_9$H$_7$N))[104] and [Cr(phen)(NCS)$_4$]$^-$ (phen = 1,10-phenanthroline)[105] are among the examples of this class. Here most of the complexes have a 1:1 stoichiometry of donor–anion ratio with donor positively charged with +1 and the half-filled Mott insulating state being stabilized. Therefore, not only magnetic anions of d-electrons but also π-electron donors have localized magnetic moments, producing π–d composite magnets. Figure 24 shows the crystal structure of (TTF)[Cr(NCS)$_4$(phen)].[105] The closest contacts are between donor and acceptor through S···S contacts of NCS and TTF, and also π-stacking between the phen ligand and TTF, producing alternating 1D chains of $S = {}^3/_2$ of Cr and $s = {}^1/_2$ of donor along the c-axis, as shown in Figure 24. Since there are no close contacts in either the a- or b-direction, it is expected that the chains behave as a 1D ferrimagnetic chain, as confirmed by the susceptibility and magnetization curves. The susceptibility obeys the Curie–Weiss law with a Weiss temperature of −24.9 K, suggesting the presence of strong antiferromagnetic interactions between donor and anion spins. The susceptibility shows an antiferromagnetic transition at $T_{\mathrm{N}} = 9.0$ K, below which a steep increase in the product of the susceptibility and the temperature indicates a ferrimagnetic feature of the ordered state[106] consistent with the crystal structure. The ferrimagnetism is confirmed from the magnetization curve shown in Figure 25. The magnetization shows a steep increase in the low field range, followed by a saturation trend at higher fields, where the saturation magnetization takes a value slightly less than $2\mu_{\mathrm{B}}$ that is the value expected from the ferrimagnetic structure ($S_{\mathrm{d}} - s_\pi = {}^3/_2 - {}^1/_2 = {}^2/_2$). The deviation from the expected saturation value is considered to come from the contribution of weak ferromagnetism, which is evidenced by the saturation behavior in the very low field as shown in the inset of Figure 25. A similar ferrimagnetic transition also appears in [M(isoq)$_2$(NCS)$_4$] complexes.[105]

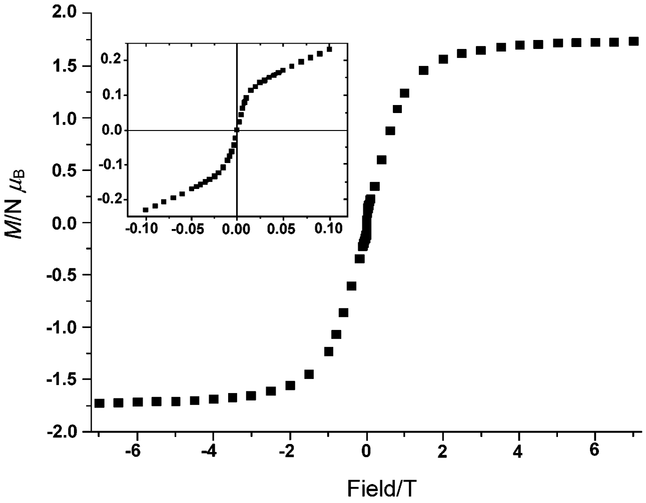

Figure 25. Magnetization curves of (TTF)[Cr(NCS)$_4$(phen)] in the ordered state. (Reproduced with permission from ref 105. Copyright 2000 Royal Society of Chemistry.)

(BDH-TTP)[M(isoq)$_2$(NCS)$_4$] (M = Cr, Fe)[107,108] is another typical example of the coexistence of ferrimagnetism and weak ferromagnetism. Figure 26 presents the crystal structure of the compound projected on the ac-plane. The donor molecules with $s = {}^1/_2$ and magnetic anions of Cr with $S = {}^3/_2$ form 1D chains along the c-axis through intermolecular S···S atomic contacts. These chains are then con-

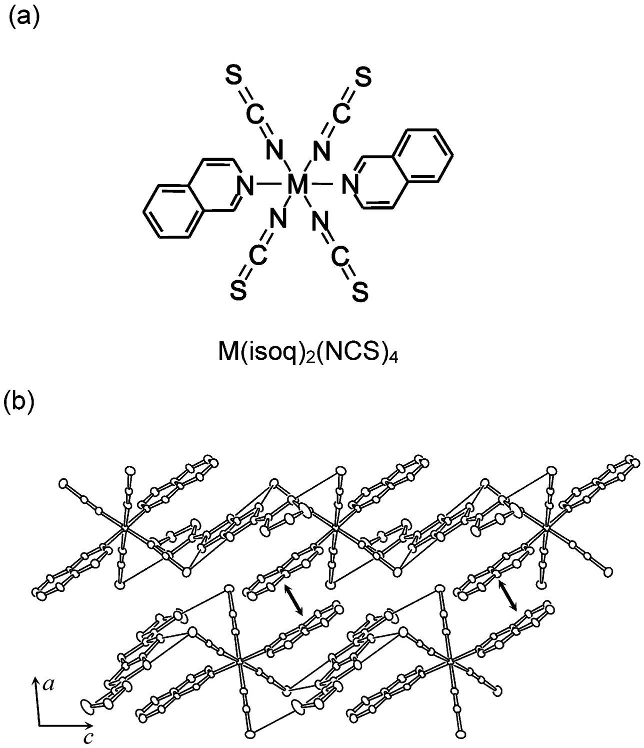

Figure 26. (a) $M(isoq)_2(NCS)_4$ molecule and (b) crystal structure of (BDH-TTP)[$Cr(isoq)_2(NCS)_4$] projected on the *ac*-plane. The solid lines are short intermolecular S···S contacts. The arrows are $\pi-\pi$ stacking between the isoquinoline ligands. (Reproduced with permission from ref 108. Copyright 2003 Elsevier.)

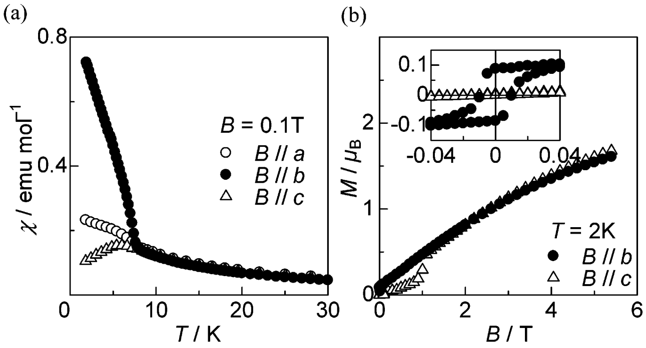

Figure 27. (a) Temperature dependence of the susceptibility of (BDH-TTP)[$Cr(isoq)_2(NCS)_4$] at $B = 0.1$ T. (b) Magnetization curves at 2 K. The inset is an expanded view around $B \sim 0$. (Reproduced with permission from ref 108. Copyright 2003 Elsevier.)

nected to each other by a $\pi-\pi$ overlap of the isoquinoline ligands of the anions. It should be noted that the CrN_6 coordinate octahedron is axially distorted along the *c*-direction and that the anions belonging to the neighboring chains are not oriented in parallel to each other, where the mutual angle between the molecular axes (defined as the isoq−Cr−isoq axis) is 5.5°. The magnetic structure is reflected by the crystal structure as shown in Figure 27 with the susceptibility and magnetization features following expected trends, as detailed below. The susceptibility shown in Figure 27a obeys the Curie−Weiss law with a Weiss temperature of −20.4 K, suggesting the presence of a rather strong antiferromagnetic interaction working between the donor and anion spins. From the magnetization shown in Figure 27b, which tends to be saturated around 2 μ_B, a ferrimagnetic spin chain structure with $s = ^1/_2$ and $S = ^3/_2$ is confirmed, where the spin easy axis is oriented along the *c*-axis, as evidenced by the appearance of a spin−flop transition at $B_{sf} \sim 1$ T. This is consistent with a steep increase and a declining trend in the susceptibility along the *b*- and *c*-axes, respectively, upon the lowering of the temperature. Interestingly, a spontaneous magnetization appears with a remnant magnetization of 0.10 μ_B along the *b*-axis, as seen in the inset of Figure 27b. This weak ferromagnetic feature is considered to be associated with the spin canting, where the canting angle is estimated as 2.9° from the saturation magnetization and the remnant magnetization. The presence of two kinds of anion sites, whose distortion axes are tilted to each other with a mutual angle of 5.5°, is responsible for the spin canting feature, though the canting angle is reduced by the contribution of the exchange interaction from the mutual angle. The coexistence of ferrimagnetism and weak ferromagnetism is also observed in the isostructural complex (BDH-TTP)[$Fe(isoq)_2(NCS)_4$],[107] where Fe has $S = ^5/_2$ in place of $S = ^3/_2$ for Cr.

6. π−d-Based Magnetic Conductors

Organic magnetic conductors have been the most highlighted among the current topics of organic conductors. The motivation of materials development in this category of magnets is based on the development of molecular versions of metal magnets. Magnetism in metallic systems or hopefully superconducting systems is expected to have unconventional features which have not appeared in traditional metal magnets with s−d interactions. Another interest is the development of ferromagnetic metals. The coexistence of metallic conductivity and ferromagnetism is attractive not only for device applications but also for basic science. In the past decade, organic ferromagnets have been discoverd.[21−23] Adding metallic conductivity to ferromagnetic molecular systems has attracted physicists and chemists as a next target. Furthermore, in the $\pi-$d systems, the interplay between electron transport and magnetism has shown interesting magnetoresistance behavior well controlled by changing magnetic structure.

Many efforts have been made for adding conducting properties to molecular magnets consisting of charge-transfer complexes, where donor and anion take part in electrical conduction and magnetism, respectively. Along these lines of the works, many interesting magnetic conductors have been developed, such as $(BEDT\text{-}TTF)_3(MnCl_4)_2$,[109] $(BEDT\text{-}TTF)_2MCo(SCN)_4$ (M = K, Rb, Cs),[110] $(EDT\text{-}TTF)_4CoCl_4(solvent)_x$,[111] $(BEDT\text{-}TTF)_3CuBr_4$,[76,85,86,91,92] $(TTM\text{-}TTP)FeBr_{1.8}Cl_{2.2}$,[112] and so forth. Among those found, there are many metallic conductors having localized magnetic moments, though all of the complexes are subjected to metal−insulator transitions. In addition, the $\pi-$d interactions in most of the materials are weak, resulting in the absence of magnetic ordering. An interesting exception is $(BEDT\text{-}TTF)_3CuBr_4$ having semiconducting features, where a strong $\pi-$d interaction mediates the exchange interaction between the d-electron spins, which brings about an antiferromagnetic transition at $T_N = 7.65$ K.[113] This is related to the employment of $CuBr_4^{2-}$ anions as d-spin source, which generates strong π−d interactions owing to the delocalized electronic feature of the d-electron state, as mentioned in the previous section. A metallic state is stabilized by the application of pressure, where a MI transition temperature is lowered upon the increase of pressure, whereas the antiferromagnetic transition temperature is elevated. Above 25 kbar, it is expected that T_N becomes higher than T_{MI}. In this situation, an antiferromagnetic metal will appear, though no experiments have been carried out so far in this connection.

(BEDT-TTF)$_3$CuCl$_4$·H$_2$O is the first organic metal, which can survive down to 200 mK, where unfortunately localized d-electron spins yield only paramagnetism with no magnetic transition.[91] The structure consists of sandwiched layers of donors and anions, where the donor forms a semimetallic electronic structure while a dimerized structure of $CuCl_4^{2-}$ is present on the anion layer. The donors and magnetic anions behave independently, as evidenced by the coexistence of donor and anion ESR signals, though there is an appreciable effect of the d-electron spins on the donor π-system. No superconductivity was observed even under high pressures up to 12 kbar.

A similar paramagnetic metallic state is found in κ-(BDH-TTP)$_2$FeCl$_4$, which does not exhibit any antiferromagnetic transition.[114]

After many efforts in the development of π−d interaction systems explained above, superconducting materials and also ferromagnetic materials have been found, which have opened the second stage of the research in organic magnetic conductors. In the next three sections, we focus on magnetic superconductors, ferromagnetic conductors, and π−d-interaction-based low-D magnetic conductors.

6.1. Magnetic Superconductors

The first discovery of superconductivity in organic magnetic conductors has been made with $T_c = 8.5$ K of (BEDT-TTF)$_4$[(H$_3$O)Fe(C$_2$O$_4$)$_3$]C$_6$H$_5$CN.[115−117] Figure 28 shows the crystal structure of this complex. The salient features of the structure are alternate layers of donors and $Fe(C_2O_4)_3^{3-}$ anions, where the donors form quasi-2D metallic sheets and $Fe(C_2O_4)_3^{3-}$ anions are arranged in a triangular 2D array with their trigonal axes perpendicular to the layer. They are separated by H$_3$O linked by hydrogen bonds to the oxygen atoms of the oxalate ions that are not coordinated to Fe. The structure of the anion layer is similar to that found in bimetallic tris(oxalate) salts with organic cations whose unusual magnetic properties have been of great interest.[118]

The resistivity as a function of temperature is presented in Figure 29. It shows a discontinuous drop to 0 at $T_c = 8.5$ K, evidencing the onset of superconductivity in this compound. The magnetoresistance also confirms the superconducting feature as shown in the inset of Figure 29. In the meantime, the susceptibility of Fe^{3+} ions obeys the Curie−Weiss law with a Weiss temperature of −0.2 K. The negligibly small antiferromagnetic interaction observed is suggestive of the absence of π−d interaction. This is the reason superconductivity appears, since the internal field present otherwise works to break the Cooper pairs.

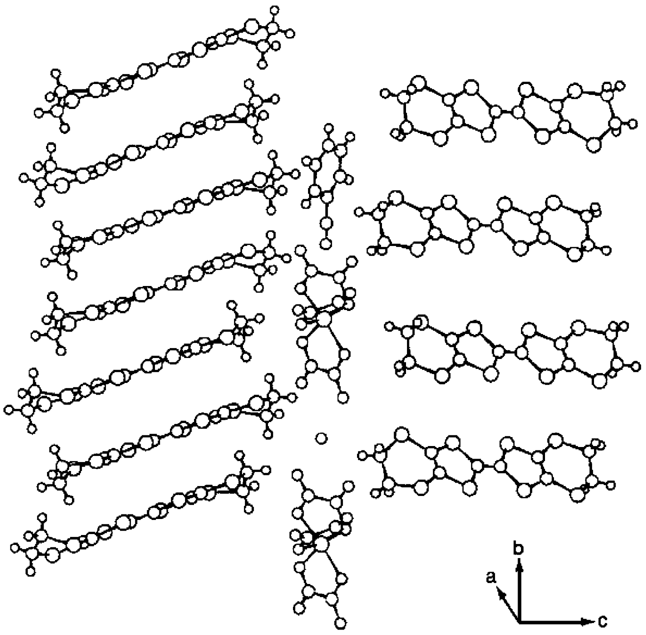

Figure 28. Molecular arrangement of (BEDT-TTF)$_4$[(H$_3$O)Fe(C$_2$O$_4$)$_3$]C$_6$H$_5$CN, showing the separation of BEDT-TTF layers by the Fe(C$_2$O$_4$)$_3$ layers. (Reproduced with permission from ref 115. Copyright 1995 Royal Society of Chemistry.)

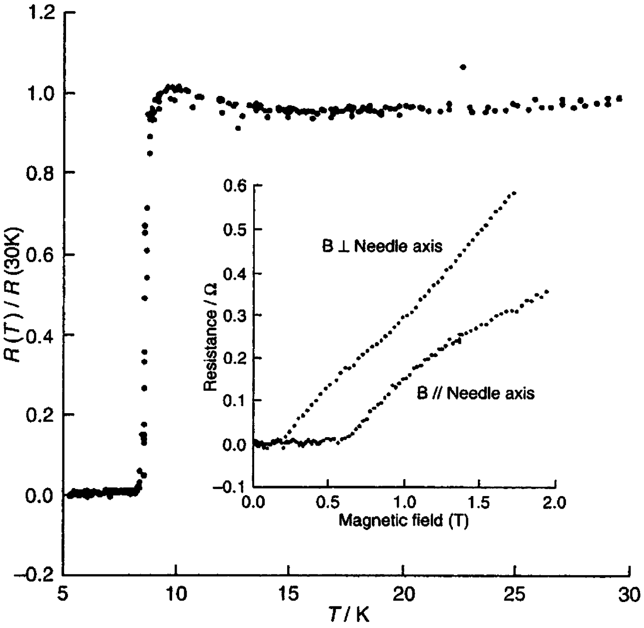

Figure 29. Temperature dependence of the resistivity of (BEDT-TTF)$_4$[(H$_3$O)Fe(C$_2$O$_4$)$_3$]C$_6$H$_5$CN. The inset shows the magntoresistance at 2 K for fields parallel and perdendicular to the needle axis. (Reproduced with permission from ref 115. Copyright 1995 Royal Society of Chemistry.)

The coexistence of a magnetically ordered phase and superconductivity has been successfully obtained in the BETS complexes with FeX$_4$ (X = Cl, Br),[119,120] which will be discussed in detail in the article of H. Kobayashi in this issue. In the crystal of λ-(BETS)$_2$FeCl$_4$, the BETS donor molecules are stacked along the a-axis and form conducting planes in the ac-plane. In the absence of the external magnetic field, the π-electronic system is an insulator below $T_{\mathrm{MI}} = 8.5$ K, at which an antiferromagnetic transition of the counteranion d-spins concomitantly takes place. This antiferromagnetic insulator state is suppressed by the application of a field of $\sim$10 T at low temperatures. Then, in the higher magnetic field region, a field-induced superconducting (FISC) state appears between 18 and 42 T when the field is applied parallel to the ac-plane,[121,122] as illustrated in the phase diagram in Figure 30a. It is worth mentioning that this FISC state is sensitive to the direction of the external field; when the magnitude of the field is close to the boundary of the FISC state ($<$20 T), a small deviation of the field direction from the c-axis causes the disappearance of the FISC state. This angular sensitivity comes from the Fulde–Ferrell–Larkin–Ovchinnikov (FFLO) state appearing on the both sides of the bulk superconducting phase. This state is characteristic of quasi-2D superconductors subjected to high magnetic fields with an anisotropic superconducting gap function,[123,124] and this state is also observed for the typical 2D molecular superconductor κ-(BEDT-TTF)$_2$Cu(NCS)$_2$.[125] In the highest field region ($>$42 T) the metallic state recovers, showing that this FISC state is not a triplet superconducting state that has, in principle, no limit on the upper critical field.

The origin of the FISC state can be explained from the Jaccarino–Peter (JP) field compensation effect,[126] which was first confirmed in Eu–Sn Chevrel-phase compounds $\sim$20 years after their prediction.[127] In the present case of λ-(BETS)$_2$FeCl$_4$, the spins $\mathbf{s}$ of the conduction π-electrons on the donors and the localized spins $\mathbf{S}$ on the counteranion are coupled with each other through an antiferromagnetic interaction as $2J_{\pi d}\mathbf{s}\cdot\mathbf{S}$. As a result, under the molecular-field treatment, the effective field H_{eff} acting on the electron spin is expressed as $H_{\mathrm{eff}} = B + (J_{\pi d}/g\mu_{\mathrm{B}})\langle S\rangle$, where $\langle S\rangle$ is the expectation value for the z-component of the anion d-spin. If $J_{\pi d} < 0$, as in the present case, the external field B can be compensated for the exchange field $(J_{\pi d}/g\mu_{\mathrm{B}})\langle S\rangle$, driving the system below the Clogston–Chandrasekhar paramagnetic limit of the upper critical field H_{c2} of the superconducting state in the high field region.[128,129] According to the temperature–magnetic field phase diagram, the external field is completely compensated by the exchange field at $B = 33$ T. The internal field of the magnetic anion acting on the conduction π-electron is also observed as the Zeeman splitting of the Fermi surface, which is detected from the quantum oscillation of the magnetoresistance (Shubnikov–de Haas effect) in the normal-metal phase.[130] From these results the magnitude of the π–d interaction can be estimated at $|J_{\pi d}| \sim 18$ K by assuming that $g = 2$ and $\langle S\rangle = {}^5/_2$ for FeCl$_4^-$ anion. The experimental result is in good agreement with the value $|J_{\pi d}| \sim 16$ K estimated from the intermolecular overlap integral obtained from the extended Hückel Hamiltonian.[99] This value of the π–d interaction is exceptionally strong among the π–d interaction-based molecular magnets. This can be regarded as a consequence of the chloride ligand of the magnetic counteranion's close proximity to the inner tetraselenafulvalene moiety of the BETS donor having large π-electron density. The magnitude of the internal field can also be controlled by changing the concentration of the magnetic anion, that is, by alloying the paramagnetic anion FeCl$_4^-$ with the diamagnetic anion GaCl$_4^-$ having the same ion size.

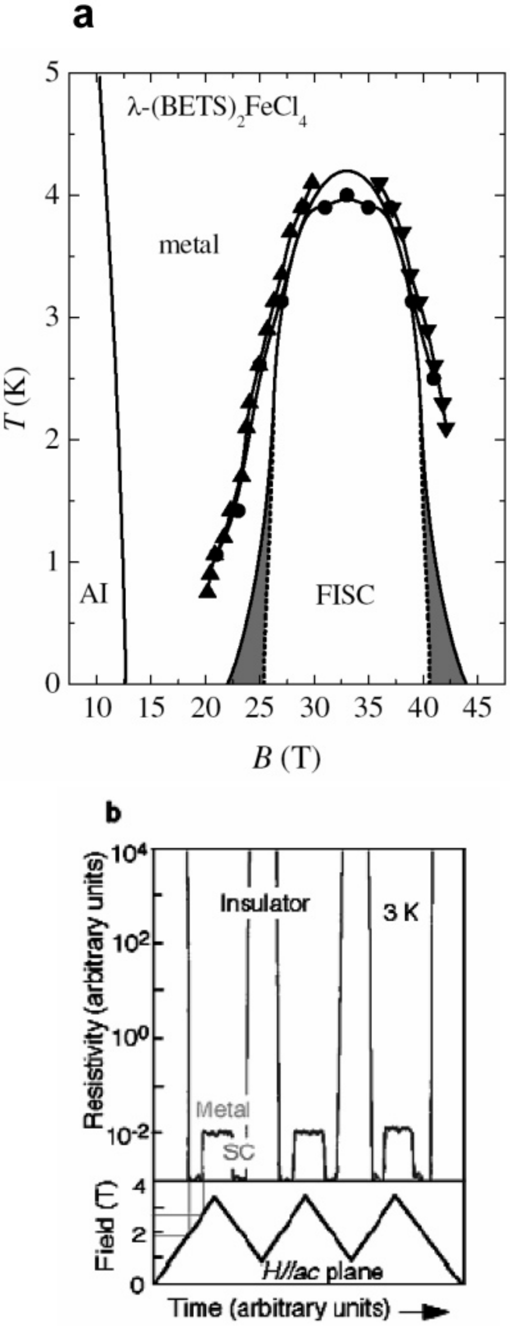

Figure 30. (a) Temperature–magnetic field phase diagram showing the antiferromagnetic insulator (AI), metallic, and FISC states for λ-(BETS)$_2$FeCl$_4$ ($B\|ac$-plane). Solid triangles and circles are phase boundaries determined from resistivity at constant temperature and magnetic field, respectively. The solid line is a theoretical fit to a phase transition toward the FISC state, while the dashed lines are transitions from the FFLO state into the bulk SC state. (Reproduced with permission from ref 122. Copyright 2001 American Physical Society.) (b) Demonstration of the insulator–superconductor–metal switching behavior coupled with the periodic modulation of magnetic field around 2.5 T ($B\|ac$-plane) at 3 K (Reproduced with permission from ref 131. Copyright 2002 American Chemical Society.)

For example, the alloy λ-(BETS)$_2$Fe$_{0.4}$Ga$_{0.6}$Cl$_4$ has a JP compensation field of ~10 T and shows successive insulator−superconductor−metal phase transitions in the low-field region around 2.5 T at 3 K, as exhibited in Figure 30b.[131] Since the resistivity changes associated with these phase transitions are quite drastic, this type of magnetic superconductor can possibly be one of the targets of novel molecular devices soon.

β-(BDA-TTP)$_2$FeCl$_4$ is another example of a magnetic superconductor.[114,132] The crystal structure consists of alternating stacking of 2D donor layers and FeCl$_4^-$ anion layers, where the donor layer has 2D Fermi surfaces similar to those of κ-(BEDT-TTF)$_2$Cu(NCS)$_2$.[133] The donors undergo an MI transition at $T_{\mathrm{MI}} = 113$ K at ambient pressure, while the d-electron spins of the anions take an antiferromagnetic transition at $T_{\mathrm{N}} = 8.5$ K. The application of pressure suppresses the MI transition and eventually induces a superconducting transition at 3 K under a pressure of 5.5 kbar.[134]

6.2. Ferromagnetic Conductors

The coexistence of a metallic state and a ferromagnetic state is one of the important issues in molecular conducting magnetic systems, which is stimulating organic electronic device applications also. It should be stressed that the presence of an interaction between the ferromagnetic system and the conducting one is particularly important in developing ferromagnetic conductors. In recent years, several interesting compounds, such as (BEDT-TTF)$_3$[MnCr(C$_2$O$_4$)$_3$],[135] (EDO-TTFI$_2$)$_2$M(mnt)$_2$ (M = Ni, Pt),[136,137] and (BO)$_3$[FeCr(C$_2$O$_4$)$_3$],[138] have been found. However, no compound could produce the interaction between the two systems. Here, among the materials having ever been obtained, two typical examples are discussed.

The first example is (EDO-TTFI$_2$)$_2$M(mnt)$_2$ (M = Ni, Pt, mnt = maleonitrile-dithiolate),[136] in which the donor metallic system interacts with the ferromagnetic anion system. The crystal structure shown in Figure 31 consists of 1D EDO-TTFI$_2$ columns of π-electron system and 1D magnetic chains of M(mnt)$_2$ anions with $S = 1/2$, which are aligned parallel to each other along the c-axis. The donor chain, which is metallic with a $3/4$ filled state and has an interlayer interaction that is 1 order of magnitude smaller than the intrachain interaction, creates a MI transition around 90 K for both M = Ni and Pt. The susceptibility shows 1D ferromagnetic features with the interaction estimated as $J \sim 20$ K, where the Ni and Pt complexes behave as Heisenberg and Ising systems, respectively, as presented in Figure 32 with theoretical fitting curves of 1D Heisenberg[139] and Ising[140] ferromagnets. The large anisotropy in the susceptibility in the Pt complex suggests the spin easy axis is oriented parallel to the (ac)-direction in the molecular plane. The origin of the ferromagnetic interaction can be explained by the unique electronic structure of M(mnt)$_2$. As the nominal valence state of the central metal atom Ni or Pt surrounded by the planar ligand is +2, the M(mnt)$_2$ does not have any localized spins in the neutral state. Charge transfer from the donor makes the anion charged with −1, where the transferred electron having $S = 1/2$ is delocalized on the whole anion molecule despite the majority of electron density populated on the central metal atom. According to molecular orbital considerations, the spin density at the central metal atom is opposite to that at the S site of the ligand. The wave function overlapping between adjacent anion molecules is governed by the intermolecular atomic S···M contacts owing to the stacking manner of slidden overlap. Consequently, the parallel spin arrangement between the central metal atoms is stabilized. The stabilization of the ferromagnetic configuration can be understood on the basis of the McConnel type II model.[141] The Heisenberg and Ising natures of the spins are associated with the difference in the contributions of the spin−orbit interaction on the central metal atoms, where the anisotropic spin state of Pt comes from a large spin−orbit interaction in contrast to the isotropic one in Ni.

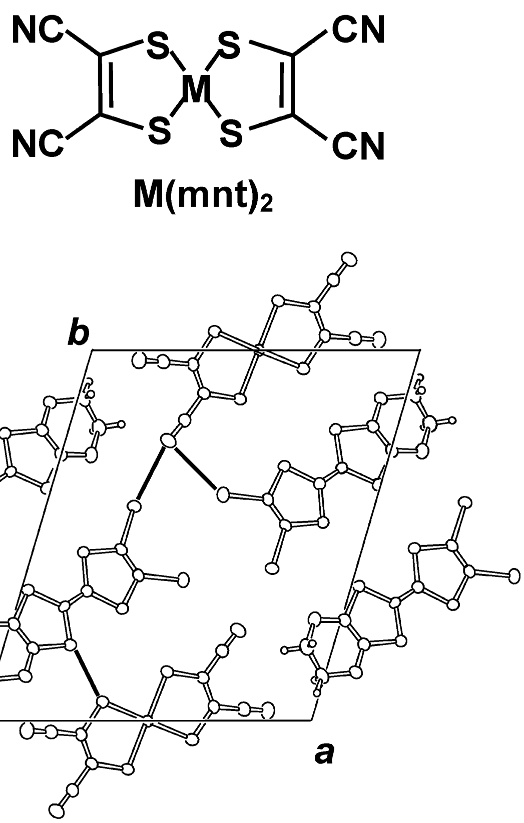

Figure 31. (top) Molecular structure of M(mnt)$_2$ and (bottom) crystal structure of (EDO-TTFI$_2$)$_2$M(mnt)$_2$ (M = Ni, Pt). Solid lines represent close atomic contacts of I···CN between donor and anion.

For the Ni complex, no magnetic long range ordering takes place down to the lowest temperature investigated (1.8 K), which is the consequence of its small magnetic anisotropy of the Heisenberg system. Here, one-dimensionality is conserved, since the interchain interaction between the adjacent magnetic anion chains is considerably small due to the lack of close intermolecular atomic contacts. In contrast, the Pt counterpart undergoes long range antiferromagnetic ordering with the spin easy axis oriented perpendicular to the chains below $T_{\mathrm{N}} = 5.5$ K, where strong magnetic anisotropy plays an important role.

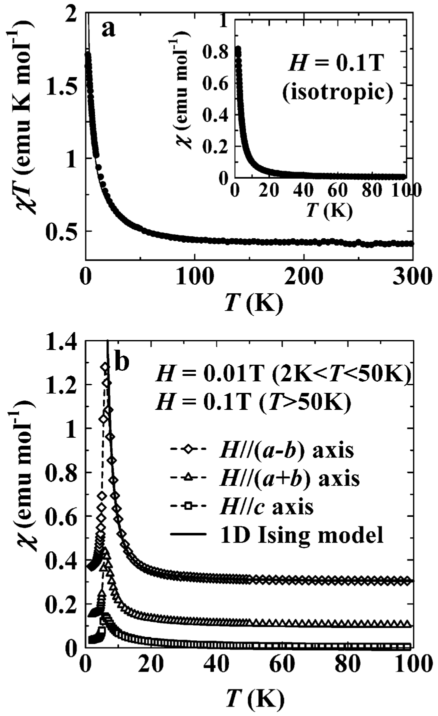

Figure 32. Temperature dependence of the susceptibility for $(EDO\text{-}TTFI_2)_2M(mnt)_2$ for M = Ni (a) and Pt (b). The solid lines are the theoretical fitting curves of $S = 1/2$ 1D Heisenberg and Ising ferromagnets with $J = 18$ and 20 K, respectively, for parts a and b. The data for the $H\|(a-b)$ and $(a+b)$ axes in part b are vertically shifted up by 0.3 and 0.1 emu/mol^{-1}, respectively, for clarity. (Reproduced with permission from ref 136. Copyright 2000 Elsevier.)

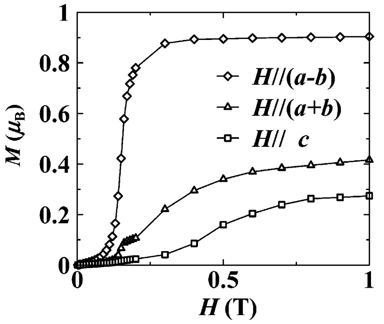

Figure 33. Magnetization curves of $(EDO\text{-}TTFI_2)_2Pt(mnt)_2$ at 3.5 K. (Reproduced with permission from ref 136. Copyright 2000 Elsevier.)

Figure 33 presents the magnetization curves at 2 K in the field parallel to the $(a-b)$-, $(a+b)$-, and c-axes. The magnetization shows a metamagnetic transition at $H_c = 0.15$ T, where weak antiferromagntic interchain interaction ($J' \sim -0.05$ K) contributes to the formation of the metamagnetic feature. The small interchain interaction confirms the well defined 1D feature of the ferromagnetic chains.

It is worth noting that the donor−anion coupling is present with the aid of the I⋯NC bonding in addition to an interdonor−anion S⋯S contact, giving rise to the interaction between conduction π-electrons and localized magnetic moments, as suggested by the structural consideration shown in Figure 31. This is evidenced by the presence of only a single ESR signal, in which contributions from both donor and anion are merged. The present system is the first example of metallic electrons interacting with a ferromagnetic system. However, ferromagnetic long range order is not stabilized due to the one-dimensionality of these materials and the metallic state cannot survive in the temperature range in which magnetic correlation becomes predominant.

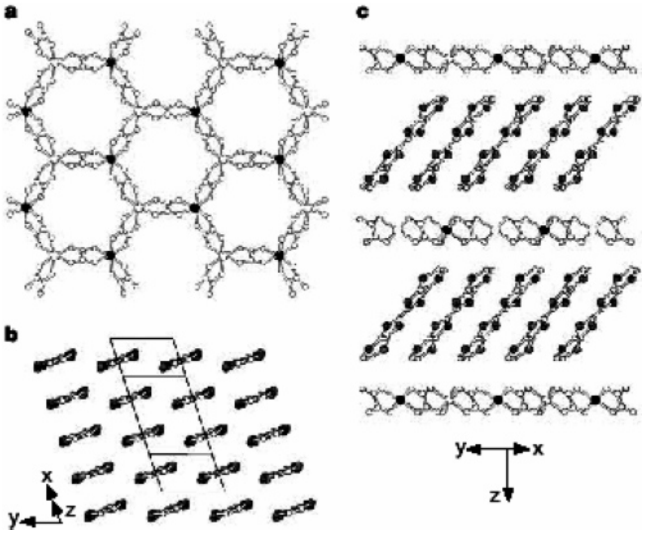

Figure 34. Crystal structure of $(BEDT\text{-}TTF)_3[MnCr(C_2O_4)_3]$. (Reproduced with permission from *Nature* (http://www.nature.com), ref 135. Copyright 2000 Nature Publishing Group.)

The coexistence of the metallic state and ferromagnetic long range order has been successfully observed in $(BEDT\text{-}TTF)_3[MnCr(C_2O_4)_3]$.[135] As shown in Figure 34, the structure of this complex consists of BEDT-TTF donor layers alternating with the honeycomb layer of the bimetallic oxalate complex $[MnCr(C_2O_4)_3]^-$. The employment of this complex is expected to give ferromagnetism, since it is known that $[M^{II}M^{III}(C_2O_4)_3]^-$ forms infinite layers of oxalate-bridged hexagonal networks, which give ferromagnetism, ferrimagnetism, or canted antiferromagnetism.[118,142] The donors form a 2D conducting sheet with a $5/6$ filled state, being suggested to be metallic. The magnetization indicates an onset of ferromagnetic long range order at $T_c = 5.5$ K, as shown in Figure 35a. The ferromagnetic nature is confirmed by the magnetization curve in the ordered state exhibited in Figure 35b, where a rapid saturation appears in the low field range with a saturation magnetization of 7.1 μ_B. The saturation value, which is slightly smaller than that expected (8 μ_B) for the sum of Mn^{2+} ($S = 5/2$) and Cr^{3+} ($S = 3/2$), is considered to come from the canted spin structure.[118] The hysteretic behavior shows a quite small coercive force $H_c \sim 0.5-1$ mT, suggesting the features of a soft magnet. The magnetic feature is similar to that already reported for other Mn(II)Cr(III)-oxalato layer magnets.[143] The large interlayer separation imposed by the insertion of BEDT-TTF donors into the bimetallic oxalate layers is considered to have no effect on the magnetic properties. The conductivity shown in Figure 36 behaves in a metallic manner down to the lowest temperature investigated (2 K) with a room-temperature value of ~250 S cm^{-1}. The application of a magnetic field perpendicular to the layers leads to the appearance of a negative magnetoresistance at

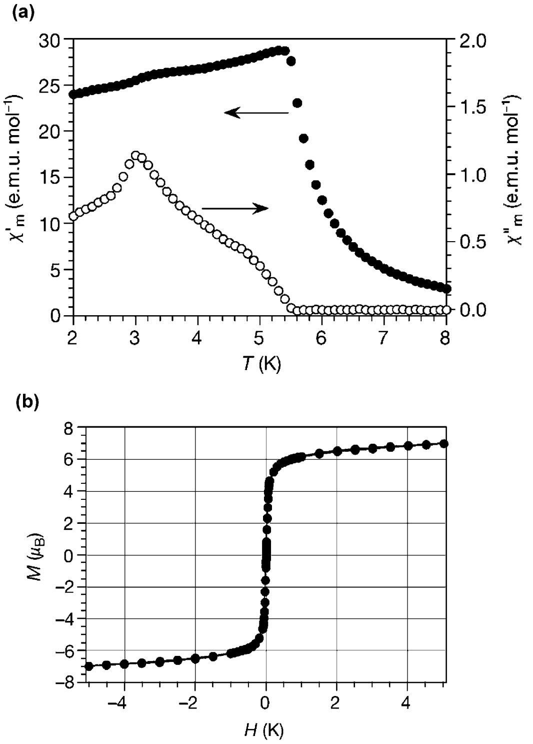

Figure 35. Magnetic characterization of (BEDT-TTF)$_3$[MnCr(C$_2$O$_4$)$_3$]. (a) Imagingry part (open circles) and real part (closed circles) of the susceptibility as a function of temperature, and (b) magnetization curve in the ferromagnetic ordered state (2 K). (Reproduced with permission from *Nature* (http://www.nature.com), ref 135. Copyright 2000 Nature Publishing Group.)

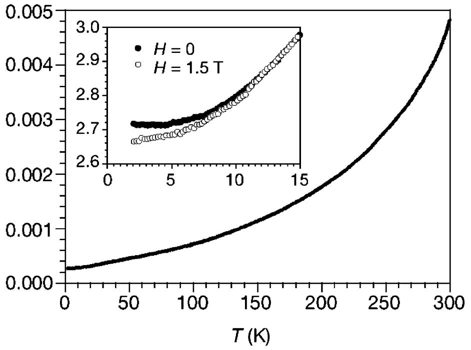

Figure 36. Temperature dependence of the resistivity of (BEDT-TTF)$_3$[MnCr(C$_2$O$_4$)$_3$]. The inset shows the magnetic field effect on the resistivity. (Reproduced with permission from *Nature* (http://www.nature.com), ref 135. Copyright 2000 Nature Publishing Group.)

temperatures below ~10 K. No influence of the metallic conducting π-electron layer exists on the magnetism of the anion. Eventually, it can be concluded that the absence of π−d interaction makes the donor π-electron system and the anion magnetic system behave independently from each other.

6.3. π−d-Interaction-Based Low-Dimensional Magnetic Conductors

Low-D conducting π-electron systems have a large variety of electronic phases, such as metal, superconductor, CDW, SDW, Mott insulating state, charge ordering state, and so forth, owing to the competition between transfer integral, on-site Coulomb interaction, intersite Coulomb interaction, and electron−phonon interaction,[24−26] as discussed in section 2. The electronic instability inherited by the low-dimensionality plays an important role in the variety of electronic phases. When we add localized d-electron spins to such π-electron systems as an additional degree of freedom, the competition and cooperation between the electronic instability and the localized d-electrons are expected to produce unconventional phenomena that do not happen in simple π-conducting systems. The field-induced superconductivity produced in λ-(BETS)$_2$FeCl$_4$[121] is one example of what happens owing to the competition. In this section, we discuss the interesting interplay between the electron transport of the π-electrons and the magnetism of d-electron spins, to which the π−d interaction essentially contributes, with (DMET)$_2$FeBr$_4$, (EDTDM)$_2$FeBr$_4$, and (EDO-TTFBr$_2$)$_2$FeX$_4$ (X = Cl, Br). We start the discussion with the first set of materials.

Isostructural quasi-1D metals (DMET)$_2$FeBr$_4$ and (EDTDM)$_2$FeBr$_4$ form a sandwich layered structure of donor π-electron conducting sheets and a magnetic lattice of d-spins of FeBr$_4^-$ anion sheets, as shown in Figure 37.[144−147] In a donor sheet on the *ab*-plane, a uniform face-to-face stacking of donor molecules constitutes a quasi-1D chain structure, while superexchange paths associated with the short Br⋯Br atomic contacts contribute to making a deformed square Fe^{3+} ($S = {}^5/_2$) magnetic lattice on an FeBr$_4^-$ anion sheet. It is worth noting that the presence of close S⋯Br atomic contacts contributes to the interaction between donor π-electron and Fe^{3+} spin.

A MI transition takes place at $T_{\mathrm{MI}} \sim 40$ and 15 K for (DMET)$_2$FeBr$_4$ and (EDTDM)$_2$FeBr$_4$, respectively, below which an SDW state is stabilized as an insulating magnetic ground state having small localized magnetic moments of π-electrons. The susceptibility, which is governed by Fe^{3+} spins, exhibits the Curie−Weiss behavior with Weiss temperatures of −5.7 and −2.8 K and Néel temperatures of $T_{\mathrm{N}} = 3.7$ and 3.0 K, for (DMET)$_2$FeBr$_4$ and (EDTDM)$_2$FeBr$_4$, respectively. The temperature dependence of the susceptibility, which is well explained on the basis of molecular field theory even down to the vicinity of T_{N}, indicates the 3D feature of the d-spin system, demonstrating the important role of the intersheet interaction between the adjacent FeBr$_4$ anion sheets, which is governed by the π−d interaction.

Figure 38a shows the magnetization curves in the field applied parallel to the easy axis (*a*-axis) and the *b*-axis taken in the magnetically ordered state in (DMET)$_2$FeBr$_4$. The easy axis magnetization has a spin−flop transition at $B_{\mathrm{sf,d}} \sim 2$ T. In addition to this, there appear two anomalies at B_1 at ~3.5 T and B_2 at ~5 T in the field applied parallel to the *a*- and *b*-axes, respectively. Indeed, the slope of the magnetoresistance versus field trace above $B_{\mathrm{sf,d}}$ is extrapolated to a negative value at $B = 0$ T. These findings are associated with the contribution of the π-electron spins to the magnetism, as confirmed by the molecular field analysis in the later discussion. Indeed, the anomaly at B_2 is assigned to the spin−flop transition $B_{\mathrm{sf},\pi}$ of the π-electron spin in the SDW state, proving that its easy spin axis oriented perpendicular to that

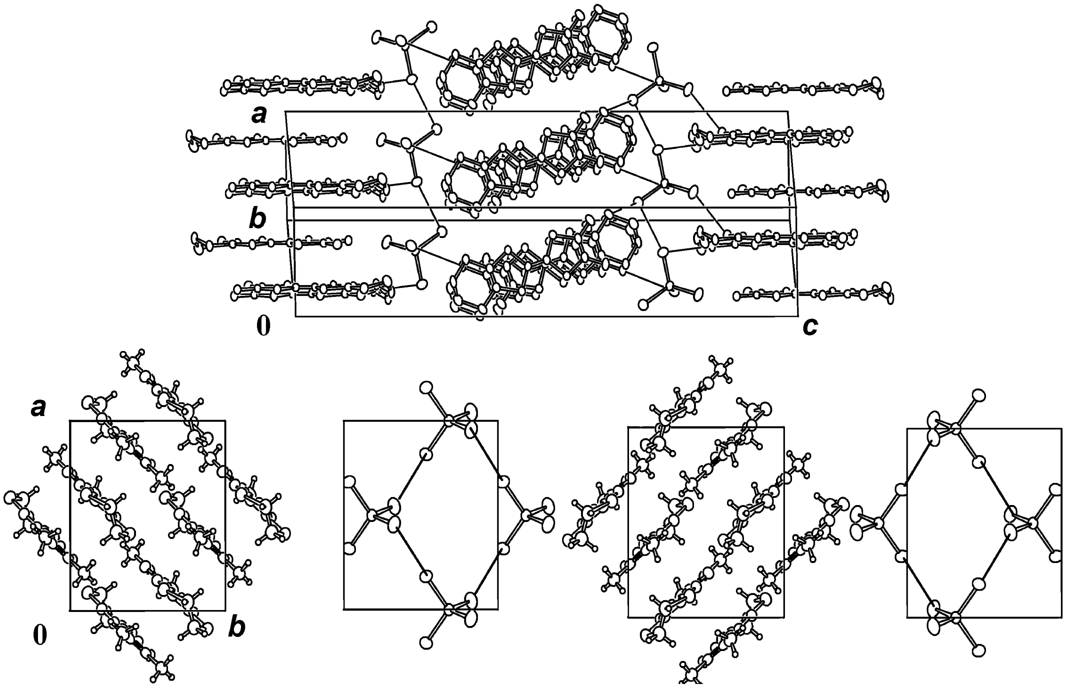

Figure 37. Crystal structure of M_2FeBr_4 (M = DMET, EDTDM). Solid lines denote close intermolecular Br···Br and Br···S atomic contacts. The projections on the *ab*-plane show the donor and the anion layers stacked sequentially.

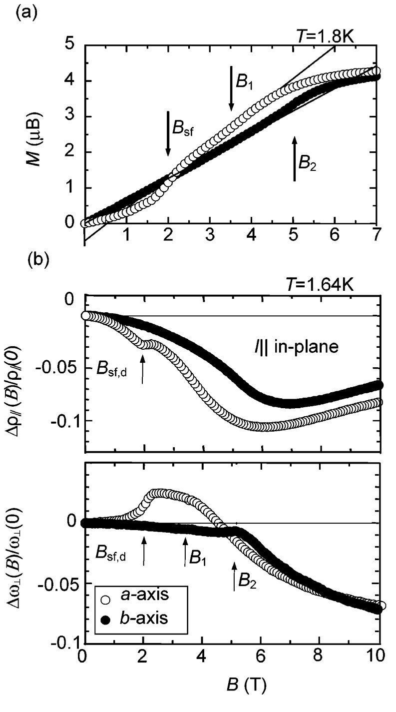

Figure 38. (a) Magnetization curves of $(DMET)_2FeBr_4$ at 1.8 K. (b) Field dependence of the magnetoresistance for the in-plane transport $\Delta\rho_{\|}(B)/\rho_{\|}(0)$ (upper panel) and the interplane hopping frequency $\Delta\omega_{\perp}(B)/\omega_{\perp}(0)$ (lower panel) in $(DMET)_2FeBr_4$ at 1.6 K. B_{sf} denotes the spin−flop transition and B_1 and B_2 show anomalies. Open and filled circles represent the data in the field applied parallel to the *a*- and *b*-axes, respectively. The solid lines in the magnetizations are fitting lines in the linear dependent regions above the spin−flop transition and below the field with anomaly B_2 in the field applied parallel to the *a*- and *b*-axes, respectively.

of the Fe^{3+} spin. The magnetoresistance tracks faithfully the magnetoresistance versus field traces, as shown in Figure 38b. The in-plane magnetoresistance $\Delta\rho_{\|}(B)/\rho_{\|}(0)$ has negative values in the whole field range investigated up to 15 T. It shows a broad minimum around 6−7 T, where the magnetization is saturated. Moreover, a discontinuous change appears at $B_{sf,d}$ for the easy axis direction. The interplane electron hopping frequency $\Delta\omega_{\perp}(B)/\omega_{\perp}(0)$ has a steep upsurge at $B_{sf,d}$ and a declining trend above B_1 in the easy axis direction, while it has a discontinuous drop at $B_{sf,\pi}$ for the *b*-axis direction or the easy axis of the π-electron spins. It becomes negative in the field range above the saturation field of the magnetization.

The excellent correlation between the magnetization and the magnetoresistance can be explained in terms of π−d interaction, taking into account that the magnetization is governed by the Fe^{3+} localized spins and the magnetoresistance reflects the electron transport of the donor π-conduction electrons. In general, in the low-temperature insulating SDW state, the generated localized spin $s_{\pi}(\mathbf{q})$ of the π-electron at nesting vector **q** is subjected to the perturbation field of the π−d interaction $\mathbf{H}_{\pi d}$ and the applied field **B**, which is given as

$$\mathbf{H}_{\pi d} + \mathbf{B} = -2z_{\pi d}J_{\pi d}\sum_{\mathbf{q}_d}\mathbf{S}_d(\mathbf{q}_d)/g\mu_B + \mathbf{B} \quad (18)$$

where $z_{\pi d}$, $J_{\pi d}$, and $\mathbf{S}_d(\mathbf{q}_d)$ are the number of nearest neighbor d-spin sites connected to the π-electron spins concerned, the π−d exchange interaction constant, and the spin operator of the Fe^{3+} d-electron having a periodicity of $\mathbf{q}_d$, respectively. Therefore, $\mathbf{s}_{\pi}(\mathbf{q})$, which is otherwise produced by the potential $\mathbf{H}_{\pi}(\mathbf{q})$ of the π-electron itself, is modified by the perturbation as given in the following equation:

$$\mathbf{s}_{\pi}(\mathbf{q}) = -\chi(\mathbf{q})[\mathbf{H}_{\pi}(\mathbf{q}) + \mathbf{H}_{\pi d}(\mathbf{q})] \quad (19)$$

where $\chi(\mathbf{q})$ is the π-electron susceptibility. In general, the periodicity $\mathbf{q}_d$ of the d-spin arrangement is not necessarily the same as that of the π-electron spins $\mathbf{q}$. However, if $\mathbf{q} = \mathbf{q}_d$, the spin polarization of the π-electron is enhanced. This contributes to increasing the SDW energy gap E_g of the insulating state, the increment of which is given by $\Delta E_{\pi d}$ in the following equation:

$$E_g = E_0 + \Delta E_{\pi d} \quad (20)$$

In contrast, the applied field B that is spatially uniform reduces the spin polarizations of the π- and d-electrons, and the application of the field, which overwhelms the energy gap, completely suppresses the insulating SDW state.

The actual case of $(DMET)_2FeBr_4$ is analyzed on the basis of a four-sublattice molecular field treatment (two Fe^{3+} spin sublattices and two π-electron spin sublattices) with π−d interaction, where the spin Hamiltonian is expressed in the following equation:

$$E_E = \frac{1}{N_u}[-2J_{dd} \sum_{\substack{\langle l,m\rangle \\ l\in d_1, m\in d_2}} \mathbf{S}_l\mathbf{S}_m - 2J_{\pi d}\sum_{i=1}^{2}\sum_{\substack{\langle l,m\rangle \\ l\in d_i, m\in \pi_i}} \mathbf{S}_l\mathbf{s}_m - 2J_{\pi\pi}\sum_{\substack{\langle l,m\rangle \\ l\in \pi_1, m\in \pi_2}} \mathbf{s}_l\mathbf{s}_m] \quad (21)$$

$$E_A = K_{ud}\{\sin^2(\theta_{d_1}) + \sin^2(\theta_{d_2})\} + K_{u\pi}\{\sin^2(\psi_\pi - \theta_{\pi_1}) + \sin^2(\psi_\pi - \theta_{\pi_2})\} \quad (22)$$

$$E_Z = g\mu_B\mathbf{B}(\mathbf{S}_{d_1} + \mathbf{S}_{d_2} + \mathbf{s}_{\pi_1} + \mathbf{s}_{\pi_2}) \quad (23)$$

$$E = E_E + E_A + E_Z \quad (24)$$

where $\mathbf{S}$ and $\mathbf{s}$ are the spins of the d- and π-electrons in the $d_{1(2)}$ and $\pi_{1(2)}$ sublattices, J_{dd} and $J_{\pi\pi}$ are the exchange interactions between d-electron spins, and between π-electron spins, respectively, K_{ud} and $K_{u\pi}$ are the magnetic anisotropy parameters for the d- and π-electron spins, respectively, and $\theta_{d_{1(2)}}$, $\theta_{\pi_{1(2)}}$, and ψ_π are the spin angles for the d- and π-electron spins, respectively, and the anisotropy direction of the π-electron spin with respect to the easy axis of the Fe^{3+} spin. By minimizing total energy E, which is given by the summation of the exchange interaction E_E, the magnetic anisotropy E_A, and the Zeeman energy E_Z, we obtain $J_{\pi\pi} = -13.5$, $J_{\pi d} = -0.2$, $J_{dd} = -0.2$, $K_{ud} = 1.3$, and $K_{u\pi} = 0.4$ K.

In the absence of an applied field, the antiparallel arrangement between the π-electron spins and the Fe^{3+} d-electron spins, where the periodicity of the Fe^{3+} spin arrangement is commensurate with that of the SDW, is stabilized due to the antiferromagnetic interaction $J_{\pi d}$, resulting in the enhancement of the SDW gap. In contrast, for the parallel spin arrangement of all the Fe^{3+} spins formed in the field of saturation, no effect is expected on the stabilization of the SDW state, since the parallel arrangement of the Fe^{3+} spins gives only a spatially uniform field to the π-electrons. Therefore, the field dependence of the in-plane resistivity $\rho_{||}(T,B)$ is expressed as follows:

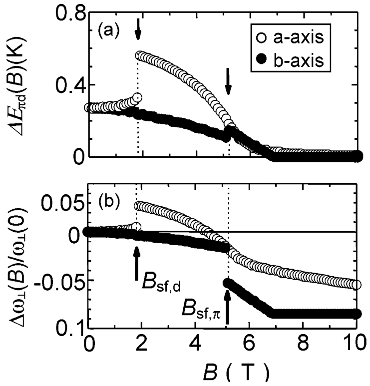

Figure 39. Applied field dependence of the contribution $\Delta E_{\pi d}$ of the π−d interaction to the SDW gap and the interlayer hopping frequency calculated for $(DMET)_2FeBr_4$. The arrows denote the spin−flop fields of the d-electron spin ($B_{sf,d}$) and the π-electron spins ($B_{sf,\pi}$). Due to the presence of the transmitting role of the susceptibility on the effect of the internal field of d-electron spins, $\Delta E_{\pi d}$ is reduced to 10% of the magnetic energy calculated. (Reproduced with permission from ref 146. Copyright 2003 The Chemical Society of Japan.)

$$\rho_{||}(T,B) \propto \exp\left(\frac{\Delta E_{\pi d}(B)}{k_B T}\right) \quad (25)$$

where $\Delta E_{\pi d}(B)$ is calculated from eqs 21−24.

The interplane electron hopping frequency is governed by the spin configuration of the half-filled Fe^{3+} d-levels, since only an electron having opposite spin to the spins of Fe^{3+} d-electrons is allowed to be transferred from one donor sheet to the adjacent sheet through Fe^{3+} d-levels according to Hund's rule. Therefore, the interlayer transfer integral becomes spin-angular dependent, as given by

$$t_{\perp i} \approx t_{0i} - t_{1i}\cos(\theta_{d_i} - \theta_{\pi_i}) \quad (i = 1, 2) \quad (26)$$

and the hopping frequency is proportional to $t_\perp$.

Figure 39 shows the applied field dependence of the SDW gap and the interlayer hopping frequency calculated. $\Delta E_{\pi d}(B)$ has anomalies at the spin−flop transitions of the Fe^{3+} spins and the π-electron spins for the a- and b-axes directions, respectively, followed by discontinuous increases, and it becomes zero above the saturation field of the Fe^{3+} spins. E_0 is estimated as 6 K from the observed resistivity, which is 1 order of magnitude larger than $\Delta E_{\pi d}(B)$. The decreasing trend of $\Delta E_{\pi d}(B)$ upon the elevation of the magnetic field is in good agreement with the observed negative magnetoresistance, where the perturbation from the Fe^{3+} internal field gives a contribution of ~10% at most to the total resistivity. The interlayer hopping frequency is also in good agreement with that observed.

The magnetoresistance in $(EDTDM)_2FeBr_4$ behaves differently from that of $(DMET)_2FeBr_4$.[145] In $(EDTDM)_2FeBr_4$, a clear MI transition takes place by applying a pressure of 9 kbar, in contrast to the case of $(DMET)_2FeBr_4$. Here the ratio of the transfer integral to the on-site Coulomb interaction is smaller in $(EDTDM)_2FeBr_4$, leading to a well-defined insulat-

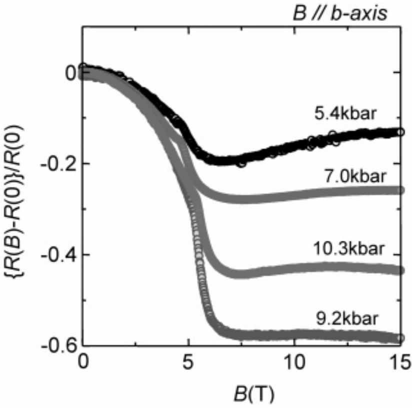

Figure 40. Pressure dependence of the magnetoresistance vs field plot at 2 K for $(EDTDM)_2FeBr_4$. (Reproduced with permission from ref 145. Copyright 2000 Taylor & Francis, Inc., http://www.routledge-ny.com.)

ing state when compared to the other complexes. Therefore, information on the electronic structure under the application of pressure lets us overlook what happens in the correlation between the magnetism and electron transport when we go from the insulating state to the metallic state in $(EDTDM)_2FeBr_4$. Figure 40 presents the pressure dependence of the in-plane magnetoresistance of $(EDTDM)_2FeBr_4$ at 2 K. The in-plane magnetoresistance exhibits similar negative magnetoresistance behavior with a minimum around the saturation field to that of $(DMET)_2FeBr_4$ in the low-pressure range. The increase in the pressure makes the magnetoresistance more negative with its value becoming field-independent above the saturation field. The largest negative magnetoresistance, whose value is almost 60%, is achieved around the critical pressure of the MI transition at ~9 kbar. Then, the negative magnetoresitance tends to be reduced when we go deeper into the metallic state. The considerable enhancement in the negative magnetoresistance in the vicinity of the MI transition is considered to be related to the effect of the 1D electronic instability taking place in the critical region taking eq 19 into account, since the susceptibility of the π-electrons at the nesting vector has divergent behavior.[99]

Another example is isostructural $(EDO\text{-}TTFBr_2)_2FeX_4$ (X = Cl, Br), which has strong π–d interactions conducive to an unconventional interplay between the electron transport and magnetism.[148,149] $(EDO\text{-}TTFBr_2)_2FeX_4$ (X = Cl, Br) has a donor–anion sandwich layered structure, as shown in Figure 41, where the Br···Br distance (3.52 Å) or the Br···Cl distance (3.40 Å) between donor and anion is almost in the range of semicovalent bonding, as evidenced by comparing with the corresponding van der Waals distance (3.70 or 3.60 Å for Br···Br or Br···Cl, respectively).[149] It should be noted that the presence of halogen atoms attached to the TTF moiety can participate in creating a strong donor–anion interaction.[150–152] Such strong and unique intermolecular Br···Br/Cl bonding is interesting not only from the point of view of structure but also for producing a strong π–d interaction. On the donor layer, a quasi-

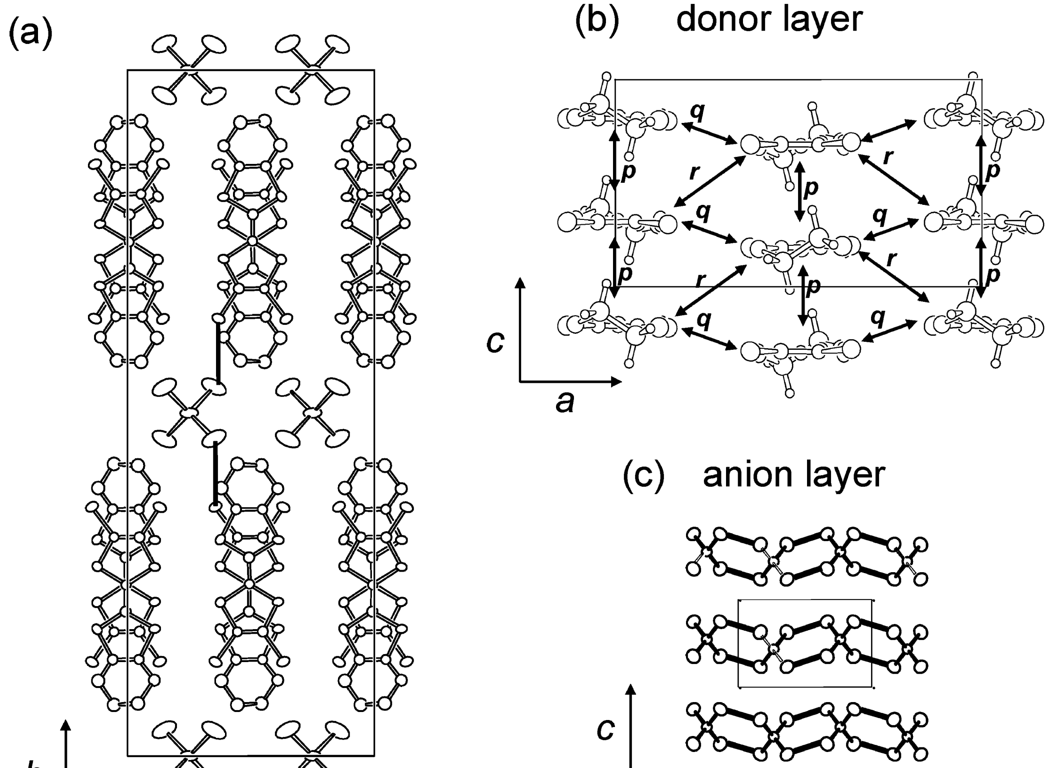

Figure 41. Crystal structure of $(EDO\text{-}TTFBr_2)_2FeX_4$ (X = Cl, Br): (a) projection on the *ab*-plane, where solid lines are close Br···Br/Cl contacts between a donor and an anion; (b) donor arrangement with transfer integrals *p*, *q*, and *r*; (c) FeX_4^- anion arrangement, where bold solid lines are close interanion X···X atomic contacts.

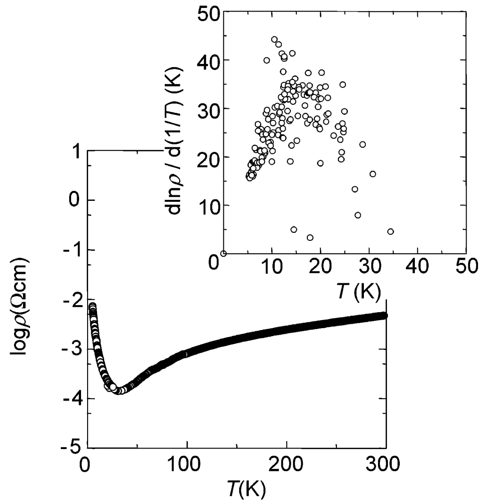

Figure 42. Temperature dependence of the in-plane resistivity ρ and the derivative of the resistivity $d \ln \rho/d(1/T)$.

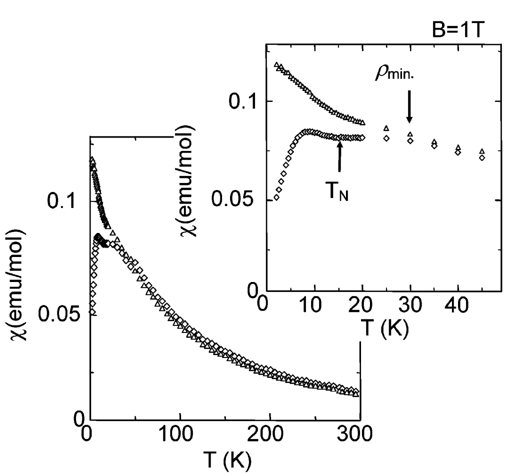

Figure 43. Temperature dependence of the susceptibility of $(EDO\text{-}TTFBr_2)_2FeBr_4$ at 1 T, where diamonds and triangles are the data taken in the fields parallel to the a- and c-axes, respectively, which correspond to the directions of the Fe^{3+} magnetic and donor chains.

1D face-to-face molecular arrangement along the c-axis direction is formed with weak side-by-side interchain interactions. Fe^{3+} d-electron spins are structured in a 1D magnetic lattice consisting of Fe−Br···Br−Fe superexchange paths along the a-axis. Interestingly, the Br···Br distance (3.87 Å) or Cl···Cl distance (4.16 Å) in the FeX_4 lattice is longer than the Br···Br/Cl distance between donor and acceptor, suggesting that the π−d interaction is expected to play an important role compared with the superexchange path within the FeX_4 magnetic sheet. Particularly, the considerably longer Cl···Cl distance indicates the absence of the superexchange path in the anion layer.

Figure 42 shows the resistivity as a function of temperature for $(EDO\text{-}TTFBr_2)_2FeBr_4$. From the resistivity, the donor π-electron system is metallic down to low temperatures with a resistivity minimum at ~30 K, where the resistivity increase below 30 K does not give any indication of gap-opening. The derivative of the resistivity shows a maximum around 15 K. Figure 43 exhibits the temperature dependence of the susceptibility for $(EDO\text{-}TTFBr_2)_2FeBr_4$. The susceptibility obeys the Curie−Weiss law with a large negative Weiss temperature of $\Theta \sim -23$ K and a magnetic moment whose value is roughly given by the contribution of Fe^{3+} ($S = 5/2$) spins. A deviation from the Curie−Weiss law gradually appears below ~150 K. The absolute value of the Weiss temperature, which is exceptionally large among the $FeBr_4^-$-including π−d interaction systems having ever been investigated, and the deviation from the Curie−Weiss law in the relatively high-temperature range suggest the presence of a strong π−d interaction, which is considered to originate from the semicovalent Br···Br bonding existing between the donor and the magnetic anion. The susceptibility shows a broad magnetic short range order plateau around 30 K, which corresponds to the temperature of the resistivity minimum. Below 30 K, magnetic anisotropy appears concomitantly with the broad plateau, where the susceptibility in the field direction parallel to the c-axis is larger than those in the a- and b-directions. Then, the susceptibility shows an upturn around 13.5 K in the a-axis direction, which is in the vicinity of the temperature of the maximum of the resistivity derivative. Finally, the susceptibility tends to decrease similarly below 8.5 K, approaching a finite value at $T = 0$ K in the field parallel to the a- and b-directions, whereas the susceptibility along the c-axis direction continuously increases. The complicated susceptibility behavior with multistage changes is suggestive of unconventional antiferromagnetic transitions taking place in the wide temperature range. Judging from the magnetization curves, which show a spin−flop transition in the a- and b-axis directions, an antiferromagnetic long range ordering transition takes place at $T_N = 8.5$ K, where the anisotropic behavior of the susceptibility is reduced upon the lowering of the temperature in the two field directions, suggestive of a helical spin arrangement in the antiferromagnetic ordered state.[153] From the structural consideration of $(EDO\text{-}TTFBr_2)_2FeBr_4$, there are multiple exchange paths in the Fe^{3+} spin system; that is, the superexchange path through the close Br···Br atomic contact within the 1D Fe^{3+} magnetic lattice and the π-conduction−electron-mediated paths through the donor−anion Br···Br contacts. The network of multiple exchange interaction paths is considered to be responsible for the helical spin system. The complicated phase transition behavior is also suggestive of the cooperation of multiple exchange interactions. In other words, the π−d interaction plays a key role in the formation of the magnetic structure of the Fe^{3+} spins. The excellent correlation between the resistivity minimum and the magnetic short range order hump gives evidence of the strong π−d interaction. For $(EDO\text{-}TTFBr_2)_2FeCl_4$, a MI transition takes place at $T_{MI} \sim 13.5$ K, while the Fe^{3+} spins undergo an antiferromagnetic transition at $T_N = 4.2$ K, below which an ordinary antiferromagnetic structure is formed with the spin easy axis oriented parallel to the a-axis. In this case, no superexchange path exists in the Fe^{3+} anion layer, and only the π−d interaction works to contribute to the antiferromagnetic ordered state.

7. Summary

TTF-type organic charge-transfer complexes, in which π-electrons play an essential role, exhibit a variety of electronic phases, such as charge density wave states, spin density wave states, Mott insulators, charge ordering states, metals, superconductors, and so on, where competitions between the transfer integral, the electron correlation, and the electron−phonon interaction give rise to electronic instabilities in their low-dimensional frames. We can also architect molecular magnets having a variety of magnetic features by intentionally employing various kinds of TTF donors and counteranions as building blocks. From magnetism aspects, in the regime where electron correlation overwhelms the transfer integral, low-D magnets appear, whereas, in the vicinity of a Mott−Hubbard metal−insulator transition with these two physical parameters competing with each other, electron conduction and magnetism coexist, owing to the spin−charge separation in highly correlated systems. In the metallic regime, where the transfer integral prevails against the electron correlation effect, magnetic systems, where a donor conduction π-electron interacts with localized spins of d-electrons, are produced by introducing counteranions having localized d-electrons. This can lead to molecular versions of metal magnets. The coexistence of d-electron spins brings about π−d composite magnets also in the insulating regime. On the basis of the schemes above, a variety of TTF-based magnetic charge-transfer complexes have been developed in four kinds of categories: (1) π-based localized magnets, (2) magnets in the Mott−Hubbard boundary, (3) π−d composite insulating magnets, and (4) π−d-based magnetic conductors, which show unconventional magnetic features different from those appearing in traditional magnetic materials. In the present paper, the magnetic properties, electronic properties, and structures of a large class of TTF-based magnetic charge-transfer complexes are comprehensively reviewed with typical examples. In the π-based localized magnets, β′-(BEDT-TTF)$_2$X (X = ICl$_2$, AuCl$_2$) are featured with quasi-2D $S = {}^1/_2$ Heisenberg antiferromagnets, (C$_1$TET-TTF)$_2$Br is a triangular antiferromagnet subjected to spin frustrations, and TTF-[M{S$_2$C$_2$(CF$_3$)$_2$}$_2$] and (TMTTF)$_2$X are spin−Peierls magnets. (TTM-TTP)I$_3$ and (EDO-TTFBr$_2$)$_3$I$_3$ show an interesting interplay between electron transport and magnetism in the Mott−Hubbard boundary with the coexistence of conduction carriers and localized spins. In the π−d composite insulating magnets, (C$_1$TET-TTF)FeX$_4$ (X = Cl, Br) are interesting examples of a triangle-based spin ladder system. Several π−d composite magnets having both π-electron spins and d-electron spins show ferrimagnetic features, in some of which spin-canting weak ferromagnetism coexists: TTF-based complexes of [M(NCS)$_4$(C$_9$H$_7$N)$_2$]$^-$ (C$_9$H$_7$N = isoquinoline) and [Cr(NCS)$_4$(phen)]$^-$ and (BDH-TTP)[M(isoq)$_2$(NCS)$_4$] (M = Cr,Fe). In the π−d-based magnetic conductors, metallic ferromagnetism appears in (BEDT-TTF)$_3$[MnCr(C$_2$O$_4$)$_3$]. In (EDO-TTFI$_2$)$_2$M(mnt)$_2$ (M = Ni, Pt), a metallic π-electron is found to interact with the ferromagnetic spin system. Superconductivity is found in (BEDT-TTF)$_4$-[(H$_3$O)Fe(C$_2$O$_4$)$_3$]C$_6$H$_5$CN, where the d-electrons show paramagnetism of localized spins. Superconductivity and antiferromagnetism coexist in κ-(BETS)$_2$FeX$_4$ (X = Cl, Br) and λ-(BETS)$_2$FeCl$_4$. Especially, a field-induced superconductivity is produced in the latter, which is the consequence of the π−d interaction. In (DMET)$_2$FeBr$_4$ and (EDTDM)$_2$FeBr$_4$, anomalous magnetic-transition-induced magnetoresistance behavior is observed owing to the π−d interaction. The presence of a strong donor−anion interaction in (EDO-TTFBr$_2$)$_2$FeX$_4$ (X = Cl, Br), which is designed intentionally for enhancing donor−anion interaction, is evidenced by a strong correlation between magnetism and electron transport.

It can be concluded that hybrid systems of charge-transfer complexes obtained based on donors and anions can easily combine functions of the constituent building blocks, leading to multifunctional materials. Intentional designing of molecular magnets based on TTF-type donors and counteranions is expected to open a new realm of magnetic materials, whose properties cannot be obtained in traditional magnetic materials.

8. Acknowledgment

This work was partly supported by a Grant-in-Aid for Scientific Research on Priority Areas of Molecular Conductors (No. 15073211) from the Ministry of Education, Culture, Sports, Science and Technology, Japan. The authors are grateful to L. Ouahab, M. Iyoda, H. Kobayashi, T. Mori, H. Mori, J. Yamada, J. Yamaura, N. Yoneyama, T. Kato, M. Enomoto, K. Enomoto, J. Nishijo, K. Okabe, H. Yamazaki, and M. Aimatsu for fruitful discussions. They would like to express their sincere thanks to B. L. V. Prasad for his fruitful suggestions about this manuscript.

9. References

(1) *Molecular Magnetism: From Molecular Assemblies to the Devices*; Coronado, E., Delhaès, P., Gatteschi, D., Miller, J. S., Eds.; Kluwer Academics Publishers: Dordrecht, 1996.

(2) Enoki, T.; Yamaura, J.-I.; Miyazaki, A. *Bull. Chem. Soc. Jpn.* **1997**, *70*, 2005.

(3) *Magnetic Properties of Organic Materials*; Lahti, P. M., Ed.; Marcel-Dekker: New York, 1999.

(4) *Molecular Magnetism, New Magnetic Materials*; Ito, K., Kinoshita, M., Eds.; Gordon and Breach Science Publishers: Tokyo, 2000.

(5) *Magnetism: Molecules to Materials*; Miller, J. S., Drillon, M., Eds.; Wiley-VCH: Weinheim, Germany, 2001.

(6) *Magnetism: Molecules to Materials II*; Miller, J. S., Drillon, M., Eds.; Wiley-VCH: Weinheim, Germany, 2001.

(7) *Magnetism: Molecules to Materials III*; Miller, J. S., Drillon, M., Eds.; Wiley-VCH: Weinheim, Germany, 2001.

(8) *Magnetism: Molecules to Materials IV*; Miller, J. S., Drillon, M., Eds.; Wiley-VCH: Weinheim, Germany, 2003.

(9) Ouahab, L.; Enoki, T. *Eur. J. Inorg. Chem.* **2004**, 933.

(10) Decurtins, S.; Gütlich, P.; Spiering, H.; Hauser, A. *Inorg. Chem.* **1985**, *24*, 2174.

(11) Gütlich, P.; Hauser, A.; Spiering, H. *Angew. Chem., Int. Ed. Engl.* **1994**, *33*, 2024.

(12) Sato, O.; Iyoda, T.; Fujishima, A.; Hashimoto, K. *Science* **1996**, *272*, 704.

(13) Kobayashi, H.; Tomita, H.; Naito, T.; Kobayashi, A.; Sakai, F.; Watanabe, T.; Cassoux, P. *J. Am. Chem. Soc.* **1996**, *118*, 368.

(14) Kobayashi, H.; Kobayashi, A.; Cassoux, P. *Chem. Soc. Rev.* **2000**, *29*, 325.

(15) Coronado, E.; Galan-Mascaros, J. R.; Gimenez-Saiz, C.; Gomez-Garcia, C. J. *Proceedings of the NATO Advanced Research Workshop on Magnetism: A Supramolecular Function*; Academic Press: New York, 1996.

(16) de Jongh, L. J.; Miedema, A. R. *Adv. Phys.* **1974**, *23*, 1.

(17) *Magnetic Properties of Layered Transition Metal Compounds*; de Jongh, L. J., Ed.; Kluwer Academic Publishers: Dordrecht/Boston/London, 1990.
(18) Sessoli, R.; Gatteschi, D.; Ganeschi, A.; Novak, M. A. *Nature* **1993**, *365*, 141.
(19) Tupitsyn, I.; Barbara, B. In *Magnetism: Molecules to Materials III*; Miller, J. S., Drillon, M., Eds.; Wiley-VCH: Weinheim, Germany, 2002; pp 109−168.
(20) Luis, F. M.; Mettes, F. L.; de Jongh, L. J. In *Magnetism: Molecules to Materials III*; Miller J. S., Drillon, M., Eds.; Wiley-VCH: Weinheim, Germany, 2002; pp 169−210.
(21) Kinoshita, M.; Turek, P.; Tamura, M.; Nozawa, K.; Shimoi, D.; Nakazawa, Y.; Ishikawa, M.; Takahashi, M.; Awaga, K.; Inabe, T.; Maruyama, Y. *Chem. Lett.* **1991**, 1225.
(22) Tamura, M.; Nakazawa, Y.; Shimoi, D.; Nozawa, K.; Hosokoshi, Y.; Ishikawa, M.; Takahashi, M.; Kinoshita, M. *Chem. Phys. Lett.* **1991**, *186*, 401.
(23) Takahashi, M.; Turek, P.; Nakazawa, Y.; Tamura, M.; Nozawa, K.; Shimoi, D.; Ishikawa, M.; Kinoshita, M. *Phys. Rev. Lett.* **1991**, *67*, 746.
(24) Williams, J. M.; Ferraro, J. F.; Thorn, R. J.; Douglas Carlson, K.; Geiser, U.; Wang, H. H.; Kini, A. M.; Whangbo, M.-H. *Organic Superconductors, Synthesis, Structure, Properties, and Theory*; Prentice Hall: Englewood Cliffs, NJ, 1992.
(25) Farges, J.-P. *Organic Conductors; Fundamentals and Applications*; Marcel-Dekker Inc.: New York, 1994.
(26) Ishiguro, T.; Yamaji, K.; Saito, G. *Organic Superconductors*; Springer: Berlin, 1998.
(27) Yoneyama, N.; Miyazaki, A.; Enoki, T.; Saito, G. *Synth. Met.* **1997**, *86*, 2029.
(28) Yoneyama, N.; Miyazaki, A.; Enoki, T.; Saito, G. *Bull. Chem. Soc. Jpn.* **1999**, *72*, 639.
(29) Yamaura, J.; Miyazaki, A.; Enoki, T.; Saito, G. *Phys. Rev. B* **1997**, *55*, 3649.
(30) Kurmoo, M.; Green, M. A.; Day, P.; Bellitto, C.; Staulo, G.; Pratt, F. L.; Hayes, W. *Synth. Met.* **1993**, *55*−57, 2380.
(31) Dumm, M.; Loidl, A.; Fravel, B. W.; Starkey, K. P.; Montgomery, L. K.; Dressel, M. *Phys. Rev. B* **2000**, *61*, 511.
(32) Laversanne, R.; Amiell, J.; Coulon, C.; Garrigou-Lagrange, C.; Delhaes, P. *Mol. Cryst. Liq. Cryst.* **1985**, *119*, 317.
(33) Emge, T. J.; Wang, H. H.; Leung, P. C. W.; Rust, P. R.; Cook, J. D.; Jackson, P. L.; Carlson, K. D.; Williams, J. M.; Whangbo, M.-H.; Venturini, E. L.; Shriber, J. E.; Azevedo, L. J.; Ferraro, J. R. *J. Am. Chem. Soc.* **1986**, *108*, 695.
(34) Kobayashi, H.; Kato, R.; Kobayashi, A.; Saito, G.; Tokumoto, M.; Anzai, H.; Ishiguro, T. *Chem. Lett.* **1986**, 89.
(35) Buravov, L. I.; Zvarykina, A. V.; Ignat'ev, A. A.; Kotov, A. I.; Laukhin, V. N.; Makova, M. K.; Merzhanov, V. A.; Rozenberg, L. P.; Shibaeva, P. P.; Yagubskii, E. B. *Bull. Acad. Sci. USSR* **1989**, 1815.
(36) Emge, T. J.; Wang, H. H.; Bowman, M. K.; Pipan, C. M.; Carlson, K. D.; Beno, M. A.; Hall, L. N.; Anderson, B. A.; Williams, J. M.; Whangbo, M.-H. *J. Am. Chem. Soc.* **1987**, *109*, 2016.
(37) Mori, T.; Inokuchi, H. *Solid State Commun.* **1987**, *62*, 525.
(38) Mori, T.; Kobayashi, A.; Sasaki, Y.; Kobayashi, H.; Saito, G.; Inokuchi, H. *Bull. Chem. Soc. Jpn.* **1984**, *57*, 627.
(39) Lines, M. E. *J. Phys. Chem. Solids* **1971**, *31*, 101.
(40) Oguchi, T. *Phys. Rev.* **1964**, *133*, A1098.
(41) Coulon, C.; Laversanne, R.; Amiell, J.; Delhaes, P. *J. Phys. C* **1986**, *19*, L753.
(42) Beno, M. A.; Firestone, M. A.; Leung, P. C. W.; Sowa, L. M.; Wang, H. H.; Williams, J. M.; Whangbo, M.-H. *Solid State Commun.* **1993**, *57*, 735.
(43) Obertelli, S. D.; Friend, R. H.; Talham, D. R.; Kurmoo, M.; Day, P. *J. Phys.: Condens. Matter* **1989**, *1*, 5671.
(44) Enoki, T.; Enomoto, M.; Enomoto, M.; Yamaguchi, K.; Yoneyama, N.; Yamaura, J.; Miyazaki, A.; Saito, G. *Mol. Cryst. Liq. Cryst.* **1996**, *285*, 19.
(45) Tokumoto, M.; Anzai, H.; Ishiguro, T. *Synth. Met.* **1987**, *19*, 215.
(46) Kobayashi, H.; Kato, R.; Kobayashi, A.; Nishio, Y.; Kajita, K.; Sasaki, W. *Chem. Lett.* **1986**, 833.
(47) Kawamura, H.; Miyashita, S. *J. Phys. Soc. Jpn.* **1984**, *53*, 9.
(48) Anderson, P. W. *Mater. Res. Bull.* **1973**, *8*, 153.
(49) Tokumoto, M.; Anzai, H.; Ishiguro, T.; Saito, G.; Kobayashi, H.; Kato, R.; Kobayashi, A. *Synth. Met.* **1987**, *19*, 215.
(50) Komatsu, T.; Sato, H.; Nakamura, T.; Matsukawa, N.; Yamochi, H.; Saito, G.; Kusunoki, M.; Sakaguchi, K.; Kagoshima, S. *Bull. Chem. Soc. Jpn.* **1995**, *68*, 2223.
(51) Kawamura, H.; Miyashita, S. *J. Phys. Soc. Jpn.* **1984**, *53*, 4138.
(52) Ajiro, Y.; Kikuchi, H.; Sugiyama, S.; Nakashima, T.; Shamoto, S.; Nakayama, N.; Kiyama, M.; Yamamoto, N.; Oka, Y. *J. Phys. Soc. Jpn.* **1988**, *57*, 2268.
(53) Blundell, S. J.; Pratt, F. L.; Pattenden, P. A.; Kurmoo, M.; Chow, K. H.; Takagi, S.; Jestädt, Th.; Hayes, W. *J. Phys.: Condens. Matter* **1997**, *9*, L119.
(54) Huizinga, S.; Kommandeur, J.; Sawatzky, G. A.; Thole, B. T.; Kopinga, K.; de Jonge, W. J. M.; Roos, J. *Phys Rev. B* **1979**, *19*, 4723.
(55) Nakazawa, Y.; Sato, A.; Seki, M.; Saito, K.; Hiraki, K.; Takahashi, T.; Kanoda, K.; Sorai, M. *Phys. Rev. B* **2003**, *68*, 085112.
(56) Meneghetti, M.; Lunardi, G.; Bozio, B.; Pecile, C. *Synth. Met.* **1991**, *41*−*43*, 1775.
(57) Jacobs, I. S.; Bray, J. W.; Hart, H. R., Jr.; Interrante, L. V.; Kasper, J. S.; Watkins, G. D.; Prober, D. E.; Bonner, J. C. *Phys. Rev. B* **1976**, *14*, 3036.
(58) Liu, Q.; Ravi, S.; Pouget, J. P.; Coulon, C.; Bourbonnais, C. *Synth. Met.* **1993**, *55*−*57*, 1840.
(59) Hase, M.; Tereasaki, I.; Uchinokura, K. *Phys. Rev. Lett.* **1993**, 70, 3651.
(60) Isobe, M.; Ueda, Y. *J. Phys. Soc. Jpn.* **1996**, *65*, 1178.
(61) Bonner, J. C.; Fisher, M. E. *Phys. Rev.* **1964**, *135*, A640.
(62) Seo, H.; Fukuyama, H. *J. Phys. Soc. Jpn.* **1997**, *66*, 1249.
(63) Fabre, J. M.; Gouasmia, A. K.; Giral, L.; Chasseau, D. *Tetrahedron Lett.* **1988**, *29*, 2185.
(64) Bourbonnais, C. *Synth. Met.* **1997**, *84*, 19.
(65) Vescoli, V.; Degiorgi, L.; Henderson, W.; Grüner, G.; Starkey, K. P.; Montgomery, L. K. *Science* **1998**, *281*, 1181.
(66) Lorenz, T.; Hoffman, M.; Grüninger, M.; Freimuth, A.; Uhrig, G. S.; Dumm, M.; Dressel, M. *Nature* **2002**, *418*, 614.
(67) Shulz, H. J. *Int. J. Mod. Phys. B* **1991**, *5*, 57.
(68) Nagaosa, N. *Quantum Field Theory in Strongly Correlated Electronic Systems*; Springer-Verlag: Berlin, 1999; Chapter 3-2.
(69) Mori, H.; Tanaka, S.; Mori, T. *Phys. Rev. B* **1998**, *57*, 12023.
(70) Mori, T.; Kawamoto, T.; Yamaura, J.; Enoki, T.; Misaki, Y.; Yamabe, T.; Mori, H.; Tanaka, S. *Phys. Rev. Lett.* **1997**, *79*, 1702.
(71) Miyazaki, A.; Kato, T.; Yamazaki, H.; Enoki, T. *Phys. Rev. B* **2003**, *68*, 085108.
(72) Yoneyama, N.; Miyazaki, A.; Enoki, T. *Bull. Chem. Soc. Jpn.* **1999**, *72*, 11.
(73) Tajima, H.; Arifuku, M.; Ohta, T.; Mori, T.; Inokuchi, H.; Misaki, Y.; Yamabe, T.; Mori, H.; Tanaka, S. *Synth. Met.* **1995**, *71*, 1951.
(74) Ajiro, Y.; Matsukawa, S.; Yamada, T.; Haseda, T. *J. Phys. Soc. Jpn.* **1975**, *39*, 259.
(75) Batail, P.; Ouahab, L.; Torrance, J. B.; Pylmann, M. L.; Parkin, S. S. S. *Solid State Commun.* **1985**, *55*, 597.
(76) Mori, T.; Sakai, F.; Saito, G.; Inokuchi, H. *Chem. Lett.* **1987**, 927.
(77) Mori, T.; Inokuchi, H. *Bull. Chem. Soc. Jpn.* **1988**, *61*, 591.
(78) Mori, T.; Wang, P.; Imaeda, K.; Enoki, T.; Inokuchi, H.; Sakai, F.; Saito, G. *Synth. Met.* **1988**, *27*, A451.
(79) Katsuhara, M.; Aragaki, M.; Mori, T.; Misaki, Y.; Tanaka, K. *Synth. Met.* **2001**, *120*, 823.
(80) Sayaduzzaman, M.; Katushara, M.; Nii, H.; Kawamoto, T.; Mori, T. *Cryst. Eng. Commun.* **2003**, *5*, 300.
(81) Tanaka, M.; Kawamoto, A.; Tanaka, J.; Sano, M.; Enoki, T.; Inokuchi, H. *Bull. Chem. Soc. Jpn.* **1987**, *60*, 2531.
(82) Tanaka, M.; Kawamoto, A.; Tanaka, J.; Sano, M.; Enoki, T.; Inokuchi, H. *Jpn. J. Appl. Phys.* **1987**, *26*, 893.
(83) Enoki, T.; Tomomatsu, I.; Nakano, Y.; Suzuki, K.; Saito, G. In *The Physics and Chemistry of Organic Superconductors*; Saito, G., Kagoshima, S., Eds.; Springer-Verlag: Berlin, 1990; p 294.
(84) Wang, P.; Mori, T.; Bandow, S.; Maruyama, Y.; Wang, X.; Chen, B.; Zhu, D.; Tsujikawa, K.; Suzuki, K.; Enoki, T. *Synth. Met.* **1992**, *49*, 253.
(85) Suzuki, K.; Yamaura, J.; Sugiyasu, N.; Enoki, T.; Saito, G. *Synth. Met.* **1993**, 56, 1741.
(86) Enoki, T.; Yamaura, J.; Sugiyasu, N.; Suzuki, K.; Saito, G. *Mol. Cryst. Liq. Cryst.* **1993**, *233*, 325.
(87) Enoki, T.; Yamaura, J.; Sugiyasu, N.; Nakano, Y.; Suzuki, K. In *New Functionality Materials, Vol. C, Synthetic Process and Control of Functionality Materials*; Turuta, T., Doyama, M., Seno, M., Eds.; Elsevier Science Publisher B. V.: Amsterdam, 1993; p 509.
(88) Enoki, T.; Enomoto, M.; Enomoto, M.; Yamaguchi, K.; Yoneyama, N.; Yamaura, J.; Miyazaki, A.; Saito, G. *Mol. Cryst. Liq. Cryst.* **1996**, *285*, 19.
(89) Miyazaki, A.; Enomoto, M.; Enomoto, M.; Enoki, T.; Saito, G. *Mol. Cryst. Liq. Cryst.* **1997**, *305*, 425.
(90) Mallah, T.; Hollis, C.; Bott, S.; Kurmoo, M.; Day, P.; Allan, M.; Friend, R. H. *J. Chem. Soc., Dalton Trans.* **1990**, 859.
(91) Day, P.; Kurmoo, M.; Mallah, T.; Marsden, I. R.; Friend, R. H.; Pratt, F. L.; Hayes, W.; Chasseau, D.; Gaultier, J.; Bravic, G.; Ducasse, L. *J. Am. Chem. Soc.* **1992**, *114*, 10722.
(92) Kurmoo, M.; Kanazawa, D.; Day, P.; Marsden, I. R.; Allan, M.; Friend, R. H. *Synth. Met.* **1993**, *55*−*57*, 2347.
(93) Kurmoo, M.; Day, P.; Allan, M.; Friend, R. H. *Mol. Cryst. Liq. Cryst.* **1993**, *234*, 199.
(94) Gomez-Garcia, C. J.; Ouahab, L.; Triki, S.; Coronado, E.; Delhaes, P. *Angew. Chem., Int. Ed. Engl.* **1994**, *33*, 223.
(95) Kurmoo, M.; Graham, A. W.; Day, P.; Coles, S. J.; Hursthouse, M. B.; Caulfield, J. L.; Singleton, J.; Pratt, F. L.; Hayes, W.; Ducasse, L.; Guionneau, P. *J. Am. Chem. Soc.* **1995**, *117*, 12209.
(96) Kurmoo, M.; Day, P.; Guionneau, P.; Bravic, G.; Chasseau, D.; Ducasse, L.; Allan, M. L.; Marsden, I. D.; Friend, R. H. *Inorg. Chem.* **1996**, *35*, 4719.
(97) Shieber, M. M. *Experimental Magentochemistry*—*Nonmetallic Magnetic Materials*; North-Holland: Amsterdam, 1967.

(98) Kosower, E. M.; Martin, R. L.; Meloche, V. W. *J. Am. Chem. Soc.* **1959**, *79*, 1509.

(99) Mori, T.; Katsuhara, M. *J. Phys. Soc. Jpn*. **2002**, *71*, 826.

(100) Enomoto, M.; Miyazaki, A.; Enoki, T. *Mol. Cryst. Liq. Cryst*. **1999**, *335*, 293.

(101) Enomoto, M.; Miyazaki, A.; Enoki, T. *Synth. Met.* **2001**, *121*, 1800.

(102) Enomoto, M.; Miyazaki, A.; Enoki, T. *Bull. Chem. Soc. Jpn*. **2001**, *74*, 459.

(103) Pati, S.; Chitra, R.; Sen, D.; Ramasesha, S.; Krishnamuraty, H. R. *J. Phys.: Condens. Matter* **1997**, *9*, 219.

(104) Turner, S. S.; Michaut, C.; Durot, S.; Day, P.; Gelbrich, T.; Hursthouse, M. B. *J. Chem. Soc., Dalton Trans*. **2000**, 905.

(105) Turner, S. S.; Le Pevelen, D.; Day, P.; Prout, K. *J. Chem. Soc., Dalton Trans*. **2000**, 2739.

(106) Kahn, O. *Molecular Magnetism*; VCH: New York, 1993.

(107) Setifi, F.; Golhen, S.; Ouahab, L.; Miyazaki, A.; Okabe, K.; Enoki, T.; Toita, T.; Yamada, J. *Inorg. Chem*. **2002**, *41*, 14.

(108) Miyazaki, A.; Okabe, K.; Enoki, T.; Setifi, F.; Golhen, S.; Ouahab, L.; Toita, T.; Yamada, J. *Synth. Met.* **2003**, *137*, 1195.

(109) Mori, T.; Inokuchi, H. *Bull. Chem. Soc. Jpn*. **1988**, *61*, 591.

(110) Mori, H.; Tanaka, S.; Mori, T. *J. Phys. I* **1996**, *6*, 1987.

(111) Mori, H.; Sakurai, N.; Tanaka, S.; Moriyama, H. *Bull. Chem. Soc. Jpn*. **1999**, *72*, 683.

(112) Katsuhara, M.; Aragaki, M.; Mori, T.; Misaki, Y.; Tanaka, K. *Chem. Mater*. **2000**, *12*, 3186.

(113) Yamaura, J.; Suzuki, K.; Kaizu, Y.; Enoki, T.; Murata, K.; Saito, G. *J. Phys. Soc. Jpn*. **1996**, *65*, 2655.

(114) Kikuchi, K.; Nishikawa, H.; Ikemoto, I.; Toita, T.; Akutsu, H.; Nakatsuji, S.; Yamada, J. *J. Solid State Chem*. **2002**, *168*, 503.

(115) Graham, A. W.; Kurmoo, M.; Day, P. *J. Chem. Soc., Chem. Commun*. **1995**, 2061.

(116) Kurmoo, M.; Graham, A. W.; Day, P.; Coles, S. J.; Hursthouse, M. B.; Caulfield, J. L.; Singleton, J.; Pratt, F. L.; Hayes, W.; Ducasse, L.; Guionneau, P. *J. Am. Chem. Soc*. **1995**, *117*, 12209.

(117) Martin, L.; Turner, S. S.; Day, P.; Guionneau, P.; Howard, J. A. K.; Hibbs, D. E.; Light, M. E.; Hursthouse, M. B.; Uruichi, M.; Yakushi, K. *Inorg. Chem*. **2001**, *40*, 1363.

(118) Tamaki, H.; Zhong, Z. J.; Matsumoto, N.; Kida, S.; Koikawa, M.; Achiwa, N.; Hashimoto, Y.; Okawa, H. *J. Am. Chem. Soc*. **1992**, *114*, 6974.

(119) Kobayashi, H.; Sato, A.; Tanaka, H.; Kobayashi, A.; Cassoux, P. *Coord. Chem. Rev*. **1999**, *192*, 921.

(120) Kobayashi, H.; Kobayashi, A.; Cassoux, P. *Chem. Soc. Rev*. **2000**, *29*, 325.

(121) Uji, S.; Shinagawa, H.; Terashima, T.; Yakabe, T.; Terai, Y.; Tokumoto, M.; Kobayashi, A.; Tanaka, H.; Kobayashi, H. *Nature* **2001**, *410*, 908.

(122) Balicas, L.; Brooks, J. S.; Storr, K.; Uji, S.; Tokumoto, M.; Tanaka, H.; Kobayashi, H.; Kobayashi, A.; Barzykin, V.; Gor'kov, L. P. *Phys. Rev. Lett.* **2001**, *87*, 067002.

(123) Fulde, P.; Ferrell, R. A. *Phys. Rev.* **1964**, *135*, A550.

(124) Larkin, A. I.; Ovchinnikov, Yu. N. *Zh. Eksp. Teor. Fiz.* **1964**, *47*, 1136.

(125) Singleton, J.; Symington, J. A.; Nam, M.-S.; Ardavan, A.; Kurmoo, M.; Day, P. *J. Phys.: Condens. Matter* **2000**, *12*, L641.

(126) Jaccarino, V.; Peter, M. *Phys. Rev. Lett.* **1962**, *9*, 290.

(127) Meul, H. W.; Rossel, C.; Decroux, M.; Fischer, Ø.; Remenyi, G.; Briggs, A. *Phys. Rev. Lett.* **1984**, *53*, 497.

(128) Clogston, A. M. *Phys. Rev. Lett.* **1962**, *9*, 266.

(129) Chandrasekhar, B. S. *Appl. Phys. Lett.* **1962**, *1*, 7.

(130) Uji, S.; Terakura, C.; Terashima, T.; Yakabe, T.; Terai, Y.; Tokumoto, M.; Kobayashi, A.; Sakai, F.; Tanaka, H.; Kobayashi, H. *Phys. Rev. B* **2002**, *65*, 113101.

(131) Zhang, B.; Tanaka, H.; Fujiwara, H.; Kobayashi, H.; Fujiwara, E.; Kobayashi, A. *J. Am. Chem. Soc.* **2002**, *124*, 9982.

(132) Yamada, J.; Toita, T.; Akutsu, H.; Nakatsuji, S.; Nishikawa, H.; Ikemoto, I.; Kikuchi, K. *Chem. Commun*. **2001**, 2538.

(133) Oshima, K.; Mori, T.; Inokuchi, H.; Urayama, H.; Yamochi, H.; Saito, G. *Phys. Rev. B* **1988**, *38*, 938.

(134) Choi, E. S.; Graf, D.; Brooks, J. S.; Yamada, J.; Tokumoto, M. *J. Phys.*, in press.

(135) Coronado, E.; Galán-Mascarós, J. R.; Gómez-Garciá, C. J.; Laulin, V. N. *Nature* **2000**, *408*, 447.

(136) Nishijo, J.; Miyazaki, A.; Enoki, T.; Ogura, E.; Takano, T.; Kuwatani, Y.; Iyoda, M.; Yamaura, J. *Solid State Commun*. **2000**, *116*, 661.

(137) Miyazaki, A.; Enomoto, K.; Okabe, K.; Yamazaki, H.; Nishijo, J.; Enoki, T.; Ogura, E.; Ugawa, K.; Kuwatani, Y.; Iyoda, M. *J. Solid State Chem*. **2002**, *168*, 547.

(138) Yamochi, H.; Kawasaki, T.; Nagata, Y.; Maesato, M.; Saito, G. *Mol. Crsyt. Liq. Cryst*. **2002**, *376*, 113.

(139) Baker, G. Ch.; Rushbrooke, G. S.; Gilbert, H. E. *Phys. Rev. A* **1964**, *135*, 1272.

(140) Ising, E. *Z. Phys*. **1925**, *31*, 2532.

(141) McConnell, H. M. *J. Chem. Phys*. **1963**, *39*, 1910.

(142) Mathioniére, C.; Nuttal, C. J.; Carling, S. G.; Day, P. *Inorg. Chem*. **1996**, *35*, 1201.

(143) Coronado, E.; Galán-Mascarós, J. R.; Gómez-Garciá, C. J.; Ensling, J.; Gütlich, P. *Chem. Eur. J*. **2000**, *6*, 552.

(144) Enomoto, K.; Miyazaki, A.; Enoki, T. *Synth. Met.* **2001**, *120*, 977.

(145) Okabe, K.; Enomoto, K.; Miyazaki, A.; Enoki, T. *Mol. Cryst. Liq. Cryst*. **2000**, *376*, 513.

(146) Enomoto, K.; Miyazaki, A.; Enoki, T. *Bull. Chem. Soc. Jpn*. **2003**, *76*, 945.

(147) Enoki, T.; Yamazaki, H.; Miyazaki, A.; Ugawa, K.; Ogura, E.; Kuwatani, Y.; Iyoda, M.; Sushko, Y. V. *Synth. Met.* **2003**, *133–134*, 501.

(148) Enoki, T.; Yamazaki, H.; Nishijo, J.; Miyazaki, A.; Ugawa, K.; Ogura, E.; Kuwatani, Y.; Iyoda, M.; Sushko, Y. V. *Synth. Met.* **2003**, *137*, 1173.

(149) Enoki, T.; Aimatsu, M.; Yamazaki, H.; Okabe, K.; Nishijo, J.; Enomoto, K.; Miyazaki, A.; Ugawa, K.; Ogawa, E.; Kuwatani, Y.; Iyoda, M.; Naumenko, O.; Sushko, Y. V. In *Organic Conductors, Superconductors and Magnets: From Synthesis to Molecular Electronics*; Ouahab, L., Yagubskii, E., Eds.; Kluwer Academic Publications: Dordrecht, 2004; p 113.

(150) Price, S. L.; Stone, A. J.; Lucas, J.; Rowland, R. S.; Thornle, A. E. *J. Am. Chem. Soc*. **1994**, *116*, 4910.

(151) Imakubo, T.; Sawa, H.; Kato, R. *J. Chem. Soc., Chem. Commun*. **1995**, *1097*, 1667.

(152) Iyoda, M.; Suzuki, H.; Sasaki, S.; Yoshino, H.; Kikuchi, K.; Saito, K.; Ikemoto, I.; Matsuyama, H.; Mori, T. *J. Mater. Chem*. **1996**, *6*, 501.

(153) Nagamiya, T. In *Helical Spin Ordering-1 Theory of Helical Spin Configurations, in Solid State Physics*; Seitz, F., Turnbull, D., Eds.; Academic Press: New York, 1967; Vol. 20, p 306.

CR0306438